Discriminating Long-QT Syndromes 1, 2 and 3 in Simulated Body Surface Potential Maps.

Master Thesis

presented by

cand. el. Maider Álvarez de Eulate

Institut für Biomedizinische Technik
Prof. Dr. rer. nat. Olaf Dössel
Karlsruher Institut für Technologie
2011

Supervisor: Dr. Ing. Gunnar Seemann

upna Universidad Pública de Navarra Nafarroako Unibertsitate Publikoa
Todos los derechos reservados
Eskubide guztiak erresalbatu dira

upna Universidad Pública de Navarra Nafarroako Unibertsitate Publikoa
Todos los derechos reservados
Eskubide guztiak erresalbatu dira

Eidesstattliche Erklärung
Hiermit erkläre ich an Eides statt, dass ich die vorliegende Diplomarbeit selbständig und ohne unzulässige fremde Hilfsmittel angefertigt habe. Die verwendeten Literaturquellen sind im Literaturverzeichnis vollständig angegeben.

Karlsruhe, den 18.08.2011

upna Universidad Pública de Navarra Nafarroako Unibertsitate Publikoa
Todos los derechos reservados
Eskubide guztiak erresalbatu dira

upna Universidad Pública de Navarra Nafarroako Unibertsitate Publikoa
Todos los derechos reservados
Eskubide guztiak erresalbatu dira

Contents

upna Universidad Pública de Navarra Nafarroako Unibertsitate Publikoa
Todos los derechos reservados
Eskubide guztiak erresalbatu dira

upna Universidad Pública de Navarra Nafarroako Unibertsitate Publikoa
Todos los derechos reservados
Eskubide guztiak erresalbatu dira

List of Figures

upna Universidad Pública de Navarra Nafarroako Unibertsitate Publikoa
Todos los derechos reservados
Eskubide guztiak erresalbatu dira

upna Universidad Pública de Navarra Nafarroako Unibertsitate Publikoa
Todos los derechos reservados
Eskubide guztiak erresalbatu dira

List of Tables

upna Universidad Pública de Navarra Nafarroako Unibertsitate Publikoa
Todos los derechos reservados
Eskubide guztiak erresalbatu dira

upna Universidad Pública de Navarra Nafarroako Unibertsitate Publikoa
Todos los derechos reservados
Eskubide guztiak erresalbatu dira

1

Introduction

1.1 Motivation

Congenital Long-QT Syndrome (LQTS) is a genetic disorder affecting the repolarization of the heart. Genes that encode for the various cardiac ion channels or regulatory proteins of these channels are mutated, which tends to prolong the duration of the ventricular action potential (APD). Thus, it leads to a propensity for ventricular arrhythmias, increasing risk of unexpected cardiac arrests. It affects up to 1 out of 2500 people and it's a common cause of sudden cardiac death among children and young population.

Currently, LQTS is classified according to 12 types of ion channel mutation (LQT1-12) but the first three, LQT1-3, are the most prevalent and most studied. LQT1 occurs in 30-35%, LQT2 in 25-30%, LQT3 in 5-10%, LQT4 in 1-2%, and LQT5 in 1% of cases. LQT6-12 are all rare.

Despite the significant increase regarding the understanding of this heart disease in the past years, some gaps related to the diagnosis and sub-typing methods are still in need to be filled. Genetic testing can be used to identify the responsible genes in patients with known disease but, as with all genetic tests, there are some important limitations to LQTS genetic testing. First of all, although since 2004 advances have enabled LQTS genetic testing to be commercially available (and thus the initially very high costs have been decreased), they're still not affordable for a significant part of the population. Besides the financial aspect, it is essential to be aware of the fact that the currently available genetic test will not be able to identify the LQTS-causing mutation in 100% of the patients (the error percentage is hovered around 25%). New technologies are continually being developed to better identify the still unknown mutations and, as these defects are characterized and validated, they must be incorporated into the commercially available testing. Therefore, it is of great importance to investigate and to develop alternative methods, in order to provide higher accuracy regarding the diagnosis and sub-typing of LQTS.

upna Universidad Pública de Navarra Nafarroako Unibertsitate Publikoa
Todos los derechos reservados
Eskubide guztiak erresalbatu dira

The experimental and clinical possibilities for studying cardiac arrhythmias in human ventricular myocardium are very limited. Animal hearts used for empirical studies may differ significantly from human hearts (heart size, heart rate, action potential shape, duration and restitution, vulnerability to arrhythmias, etc.) and cardiac arrhythmias are three-dimensional phenomena whereas experimental observations are still largely constrained to surface recordings. For these reasons, over the last 50 years observational cardiac electrophysiology has been increasingly complemented by computational models of membrane excitability. The mentioned models, combined with computer simulations can be used to test and generate hypotheses that are difficult to address experimentally.

1.2 Objectives and Outline

The objective of this work is to investigate alternative methods to distinguish between the first three types of the Long-QT syndrome by looking for differences in simulated Body Surface Potential Maps (BSMP). Research in this area would provide a better understanding of the voltage distribution affected by the mutations. A model of human ventricular myocytes was adapted to represent the behavior of the mutated channels and BSMP were simulated including the subtypes.

Chapter two illustrates the heart structure both microscopically and macroscopically, giving a short introduction on cardiac anatomy and electrophysiology in order to provide the basics to get a better understanding of the theory behind this project.

The Long-QT syndrome is described in chapter three. After an overview, channel kinetics and mutations behind this pathology are detailed for each of the studied subtypes. Current diagnosis methods are also explained and disadvantages are exposed.

The methods and procedures followed in this study are explained in depth in chapter four. Starting with electrophysiological modeling until BSPM simulation all the techniques and processes that were carried out are described together with the necessary mathematical background. That leads to chapter five, where all the obtained results are displayed.

Finally, chapter 6 provides a summary of the project and chapter 7 describes the limitations of this work and points out perspectives for future investigations.

upna Universidad Pública de Navarra Nafarroako Unibertsitate Publikoa
Todos los derechos reservados
Eskubide guztiak erresalbatu dira

2

Cardiac Anatomy and Electrophysiology

2.1 Cardiac Anatomy

The human heart is a muscular organ that provides a continuous blood circulation through the cardiovascular system, which is designed to transport oxygen and nutrients to the cells and remove carbon dioxide and metabolic waste products from the body. It is located obliquely in the chest behind the body of the sternum and adjoining parts of the rib cartilages, and projects farther into the left than into the right half of the thoracic cavity. The human heart is about the size of a fist and its weight varies from 230 to 340 grams, depending on the gender, being female hearts usually less heavy than male hearts.

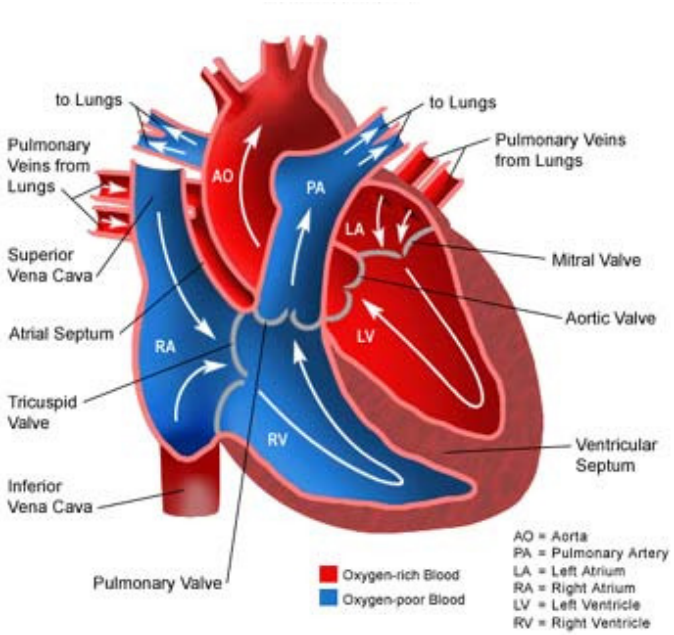

Fig. 2.1. Schematic description of the heart anatomy. [1]

upna Universidad Pública de Navarra Nafarroako Unibertsitate Publikoa
Todos los derechos reservados
Eskubide guztiak erresalbatu dira

A thick wall of muscle denominated septum separates the right and left halves of the organ and those are at the same time subdivided into 2 cavities each. Thus, the heart is divided in 4 chambers: the two upper ones are called right and left atria, whereas the two lower chambers are called right and left ventricles. The right ventricle and the right atrium are separated by the tricuspid valve, allowing the atrium to fill the ventricle with blood collected by the Vena cava superior and the Vena cava inferior. Similarly, the left ventricle and the left atrium are separated by the bicuspid valve and the blood has to to pass the aortic valve to get into the body circle via the aorta. The function of the right side of the heart is to collect de-oxygenated blood, in the right atrium, from the body and pump it, via the right ventricle, into the lungs so that carbon dioxide can be dropped off and oxygen picked up. The left side collects oxygenated blood from the lungs into the left atrium. From the left atrium the blood moves to the left ventricle which pumps it out to the body via the aorta by contractions. These contractions occur regularly and at the rate of about seventy per minute. Each wave of contraction or period of activity is followed by a period of rest, the two periods constituting what is known as a cardiac cycle. Each cardiac cycle consists of three phases, which succeed each other as follows: a short simultaneous contraction of both atria, termed the atrial systole, followed, after a slight delay, by a simultaneous but more prolonged contraction of both ventricles named the ventricular systole, and a period of rest during which the whole heart is relaxed.

The muscular wall of the heart consists of three different layers: the epicardium, the protective inner layer, underlies the myocardium, the actual muscle, which is followed by the outer layer called epicardium. The heart is surrounded by a small amount of fluid enclosed by a fibrous sac: the pericardium.

2.2 Cell Physiology

2.2.1 The Cell Membrane

The cell membrane of a cardiomyocyte is also called sarcolemma and it consists of a phospholipid bilayer. The bilayer structure is attributable to the special properties of the lipid molecules, which cause them to assemble spontaneously, due to a polar head group and two hydrophobic hydrocarbon tails [2]. The main function provided by the membrane is being a barrier for diffusion. Unlike other lipid bilayers, proteins such as receptors, pumps and channels are also contained in the sarcolemma, essential fact to the contractile process of the myocyte [3]. The ionic concentration is established by the flow of sodium (Na+), potassium (K^+), calcium (Ca^{2+}), and chloride (Cl^-) ions through the bilayer and these flows are controlled by those proteins. Figure 2.2 depicts a schematic description of the membrane including channels, pumps and receptors.

upna Universidad Pública de Navarra Nafarroako Unibertsitate Publikoa
Todos los derechos reservados
Eskubide guztiak erresalbatu dira

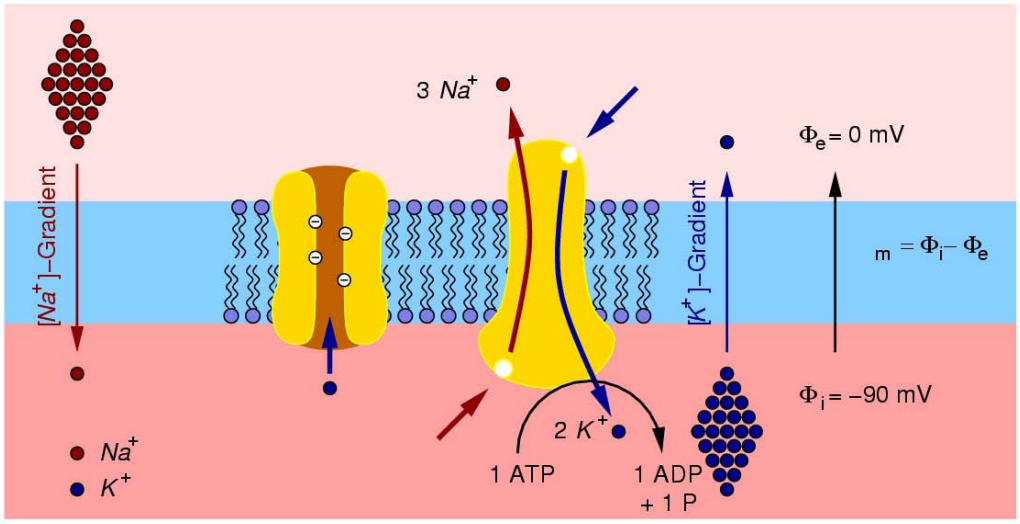

Fig. 2.2. Schematic description of the cell membrane including ionic exchangers and pumps. Different concentrations of potassium (blue circles) and sodium (red circles) in the intra- and extracellular space lead to concentration gradients across the cell membrane (thin arrows). The transmembrane proteins describing K^+ channel and Na^+ -K^+-pump are represented in yellow. Adapted from [4]

2.2.1.1 Ion Channels

As mentioned, ion channels are proteins that the sarcolemma contains. They regulate the flow of ions through the membrane controlling its selective permeability, due to the fact that they are specific regarding the different ion types. Various subunits construct these ion channels and these subunits are expressed by several genes. The α subunit is in charge of forming the channel itself, whereas the β and γ subunits modulate its function.

The mechanism of controlling the ionic flow is called gating. The ionic channels have different configurations: open, closed or inactivated, being the open state the only one in which ions are conducted. Different types of stimuli regulate the gating. In the so called voltage gated channels, voltage sensors sense certain changes in the transmembrane voltage provoking the switching of states. In other cases, specific ligands, namely acetylcholine (ACh) or adenosine triphosphate (ATP) have the ability to manage this feature, hence their name: ligand gated channels.

2.2.1.2 Pumps

Energy transformation also leads to ionic transportation through the cell. Ion pumps or ATPases perform ATP or ADP hydrolysis and consequently obtain the energy needed for the process. In the sarcolemma the Na^+ -K^+ - and the Ca^{2+} -pump are the main contributors for the active transport. The Na^+, K^+ ATPase is pumping three Na^+ ions out of the cell and at the same time two K^+ ions into it. This conducts to an ion concentration gra-

upna Universidad Pública de Navarra Nafarroako Unibertsitate Publikoa
Todos los derechos reservados
Eskubide guztiak erresalbatu dira

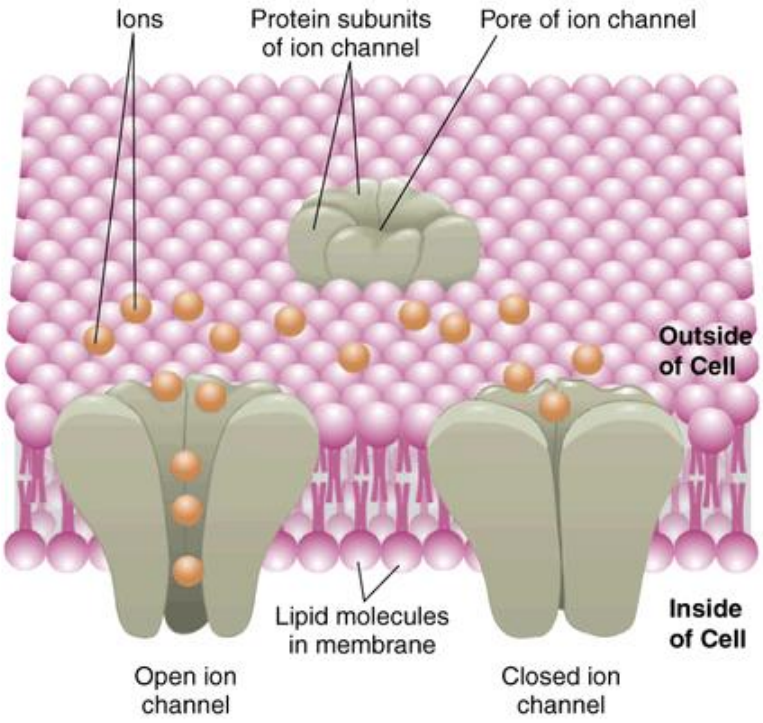

Fig. 2.3. Schematic representation of several ionic channels in the sarcolemma and with different configurations. From [5]

dient between intra- and extracellular space, which mantains the resting transmembrane voltage and, therefore, the excitability of the cell.

2.2.1.3 Exchangers

Ion exchangers allow transport against the gradient but don't require the use of external energy. They use the passive transfer of an ion type as a carrier by coupling the desired substance. If the substance is transported in the same direction as the forcing ion type, the transport mechanism is termed symport, otherwise it is named antiport. One of the most important exchangers when it comes to cardiac electrophysiology is the Na^{+}-Ca^{2+}. This exchanger regulates the distribution of Ca^{2+} in the inner and outer fluid. This distribution is imperative for the cardiac contraction.

2.2.1.4 Gap Junctions

Neighboring cells present coupling regions called intercalated discs. At these regions, low resistance pores are formed by proteins of adjacent cells: the so called gap-junctions [6]. These junctions allow for direct transport of substances between cells i.e they are not selective to specific ions and metabolites. This leads to a rapid propagation of the action

upna Universidad Pública de Navarra Nafarroako Unibertsitate Publikoa
Todos los derechos reservados
Eskubide guztiak erresalbatu dira

potential.

Gap junctions consist of connexons, which are formed by six protein subunits called connexins. Different types of connexins exist in the cardiac tissue, each of them presenting different values of unitary conductances. Moreover, the distribution of gap junctions throughout the heart is not homogeneous.

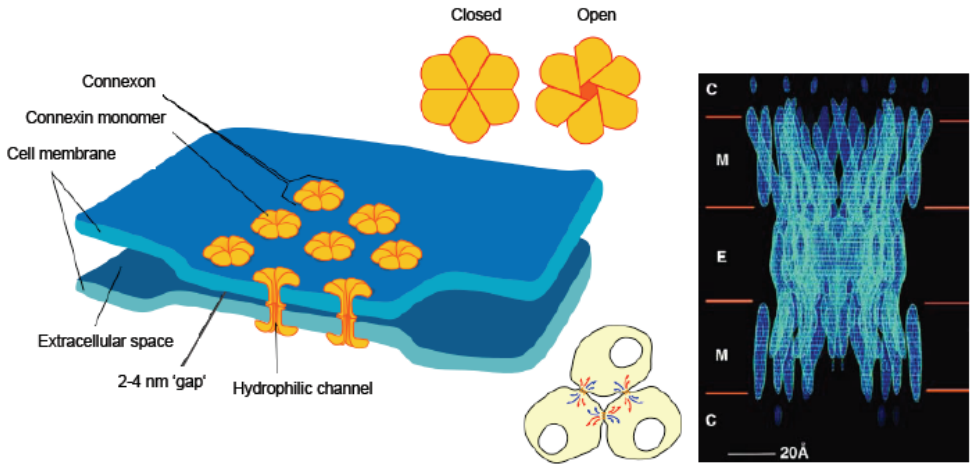

Fig. 2.4. Schematic representation of gap junctions. a) Six connexins form the connexon and two connexons are coupled to build the gap junction. b) Molecular organization of a gap junction.'E' extracellular gap,'M' membrane area, 'C' cytoplasmic space. From [7] and [8]

2.2.2 Ion Diffusion

Diffusion of ion is the most important of the so called passive transport mechanisms. No energy is required for this process, hence its classification as passive. When different molecule concentrations exist in different locations, molecules will move from the most to the least populated zone, compensating the original gradient. Fick's diffusion law describes the diffusion rate in a selective-permeable membrane:

$$J_{diff} = AD\frac{\Delta C}{\Delta x} \tag{2.1}$$

Where A is the area where the diffusion takes place, D the diffusion coefficient according to the Stokes-Einstein equation, Δ C the concentration difference between two zones, and Δ x the thickness of the membrane. Therefore, the thinner the membrane is, the most effective the transport via diffusion.

upna Universidad Pública de Navarra Nafarroako Unibertsitate Publikoa
Todos los derechos reservados
Eskubide guztiak erresalbatu dira

If the transported molecules are electrically charged, i.e ions, the electrical gradient is changed when the particles pass through the membrane, creating a potential difference which leads to an electrical driving force affecting the ions (see equation 2.2). This force can be calculated given a potential difference U and the valence z_x of the ion X.

$$F_m = z_x \frac{U}{\Delta x} \tag{2.2}$$

The total flux is the sum of the flux caused by diffusion and the flux caused by electrical forces. When it equals zero, an electrochemical equilibrium is reached and, in this situation a concentration difference of ion type X exist between intra- and extramembrane making it possible to calculate the equilibrium voltage via the Nernst equation:

$$E_x = \frac{-RT}{z_x F} \ln \frac{c_{in,x}}{c_{out,x}} \tag{2.3}$$

with F being the Faraday constant, and $c_{out,x}$ and $c_{in,x}$ being the extra- and intracellular concentrations, respectively.

2.2.3 Electrical Properties of the Cell Membrane

2.2.3.1 Resting Voltage

As previously described, the electrical gradient is changed when the particles pass through the membrane, creating a potential difference between intra- and extracellular locations. This voltage is called transmembrane voltage. Despite the fact that cells can have different transmembrane voltages, only the equilibrium voltage is called resting voltage. This resting voltage can be obtained by the Goldman-Hodgkin-Katz equation, which is an extension of the Nerst equation to take into account different ions:

$$V_m = \frac{-RT}{z_x F} \ln \frac{P_{K,c_{in,K}} P_{Na,c_{in,Na}} P_{Cl,c_{in,Cl}}}{P_{K,c_{out,K}} P_{Na,c_{out,Na}} P_{Cl,c_{out,Cl}}} \tag{2.4}$$

P_{K,c_K}, P_{Na,c_K} and P_{Cl,c_K} express the permeability for potassium, sodium and chlorine ions respectively. A more exhaustive description of the transmembrane voltage is achieved by including Ca^{2+} and the charge transport resulting from the exchangers in equation 2.4.

2.2.3.2 Action Potential

The action potential (AP) is the process that is initiated when the transmembrane voltage elevates due to an external stimuli and it is fundamental for the transmission of information through electrically active cells. When the transmembrane voltage exceeds a certain threshold, usually around -40 or -60 mV, the Na^+ channels open, causing a fast upstroke in the action potential. This opening leads to an inflow of I_{Na}, resulting on a rapid depolarization (Phase 1 in figure 2.5) where the voltage moves towards the Na equilibrium

upna Universidad Pública de Navarra Nafarroako Unibertsitate Publikoa
Todos los derechos reservados
Eskubide guztiak erresalbatu dira

potential. Around 10ms after, the transient outward potassium current, I_{to}, makes the voltage decrease to near 0 mV and leads to an early rapid repolarization. This is followed by the opening of calcium channels acting against repolarization forces, which causes the voltage to stabilize and remain nearly constant; the Plateau phase (Phase 2). The calcium influx is responsible for initiating the contraction of the myocyte. Finally, delayed voltage dependent potassium channels or "delayed rectifiers" release I_{Ks}, I_{Kr} and I_{Kur} (slow, rapid and ultra rapid delayed potassium currents respectively) which are responsible for the rapid repolarization (Phase 3). The return to resting voltage is achieved thanks to the inward rectifier K^+ current I_{K1} (Phase 4).

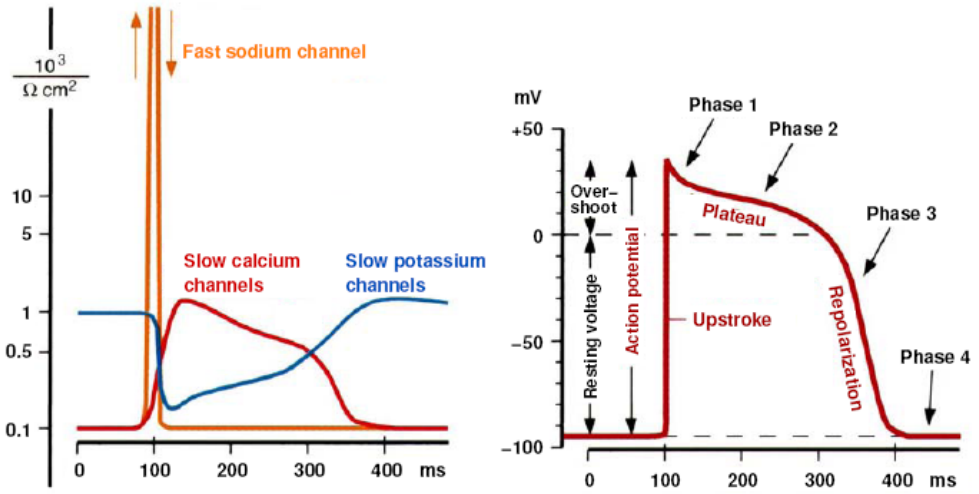

Fig. 2.5. The principal flux of the various ionic currents and the resulting action potential of a cardiac myocyte[9]

2.2.3.3 Refractory Period

After depolarization, further APs are unachievable due to Na^+ channel inactivation. The period of time in which those channels remain inactivated is called refractory period, and it has two different phases: absolute (when no matter how strong the stimulus is, the channels are completely inactive) and, immediately after, relative (new depolarization is generally possible, but with lower magnitude and a shorter duration). The refractoriness of a cell is dependent on the action potential duration (APD) since the refractory period ends when the cell membrane reaches the equilibrium voltage.

upna Universidad Pública de Navarra Nafarroako Unibertsitate Publikoa
Todos los derechos reservados
Eskubide guztiak erresalbatu dira

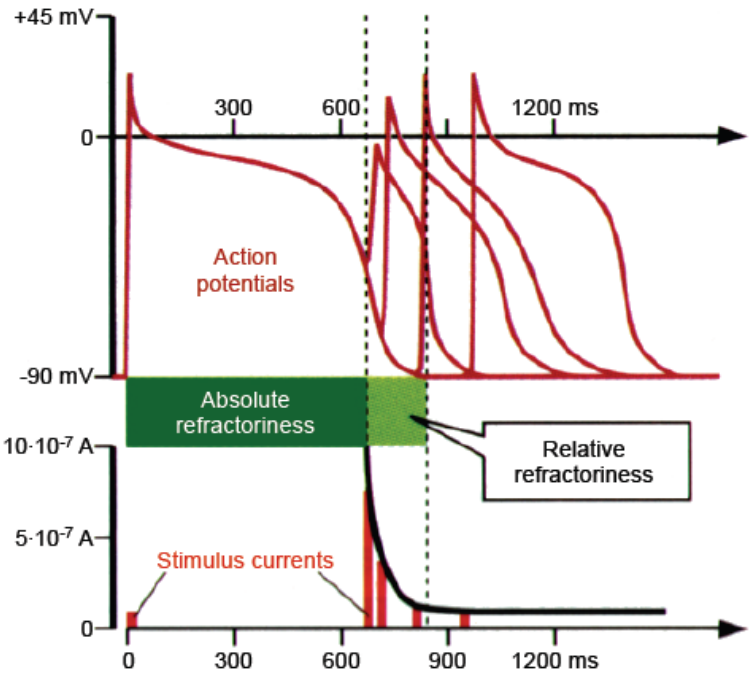

Fig. 2.6. The refractory period and its phases: absolute and relative refractoriness. During the first, no action potential is initiated, whereas during the second new depolarization is possible but with lower magnitude and shorter duration. Adapted from [4]

2.2.4 Electrical Conduction System

The propagation of the cardiac excitation is vital for the correct pumping of the heart. The atria are the first to depolarize, and the excitation reaches the complete ventricular muscle around 120ms after. The process can be seen in figure 2.7.

The sinus node, a region of the right atrium muscular tissue, is the origin of the excitation and the pacemaker. Other potential pacemakers exist in the human heart but they only have that function if the sinus node fails to perform its task. Once the excitation starts, it travels through the crista terminalis and the pectinate muscles, allowing with this the depolarization of the right atrial myocardium. It also continues into the Bachmann bundle to the left atrium, until the whole atrium is activated. The impulse continues throughout the atrioventricular node (AV), which is the only point of electrical contact between atria and ventricles. Here, the excitation suffers a delay of approximately 100ms in order to synchronize the temporal sequence. This delay is of great importance, since it allows a complete ventricular filling.

After the delay in the AV, the stimulus is conducted to the Purkinje fibers through the His and the Tawara bundles, leading then to a complete depolarization of the ventricular tissue.

upna Universidad Pública de Navarra Nafarroako Unibertsitate Publikoa
Todos los derechos reservados
Eskubide guztiak erresalbatu dira

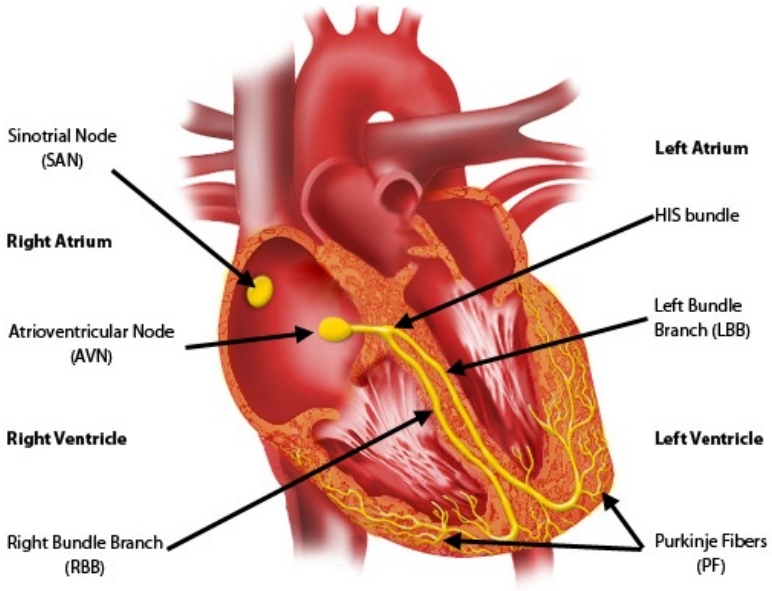

Fig. 2.7. The electrical conduction system of the heart. From [10]

2.3 The Electrocardiogram

To allow an understanding of the conduction system, an interpretation of the electrical activity is recorded via electrodes attached to the skin and located across the thorax [11]. That recording is called Electrocardiogram (ECD).

A regular ECG "drawing" consists of a P wave, a QRS complex, a T wave and a U wave, although only in the 50 to 75% of ECGs is this U wave visible[12]. The P wave represents the depolarization of the atrial myocardium, whereas the QRS complex reflects the rapid depolarization of the right and left ventricles. The higher ventricular mass is what causes the QRS complex to be significantly higher than the P wave. The T wave stands for the ventricular repolarization and the U wave is believed to be caused by the repolarization of the interventricular septum [13].

2.3.1 The T Wave

As we mentioned above, the T wave represents ventricular repolarization. In humans, the T wave usually appears to be concordant with the QRS complex and it is commonly accepted that dispersion of repolarization (DOR) is responsible for this concordance [15]. For this reason it is important to investigate the impact of the DOR in the T wave so that we get a better understanding of its morphology. In this work we intend to do so, as explained in section 4.3.

upna Universidad Pública de Navarra Nafarroako Unibertsitate Publikoa
Todos los derechos reservados
Eskubide guztiak erresalbatu dira

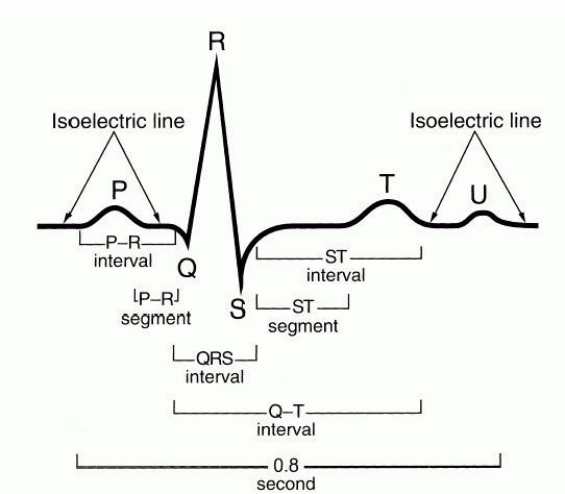

Fig. 2.8. The ECG and its different waves and segments. From [14]

upna Universidad Pública de Navarra Nafarroako Unibertsitate Publikoa
Todos los derechos reservados
Eskubide guztiak erresalbatu dira

3

Long-QT Syndrome

3.1 Overview

Generally speaking, the Long-QT Syndrome is a genetic disorder affecting the repolarization of the heart, and it has an autosomal-dominant inheritance pattern. [16]. As its self-explanatory name indicates, the Long-QT Syndrome is characterized by a prolongation of the QT time in the ECG. Differences can also be noticed among different parameters such as shape or duration of the T-wave [17]. The QT interval indicates the duration of ventricular depolarization and repolarization, which is caused by transmembrane flow of ions. Measuring this time, though, is harder than what one would expect. For instance, the interval varies with the heart rate [18] and it is difficult to determine what to measure due to the fact that the T-wave changes among individuals. A way to reach a standarized criterium is the so called corrected QT time or QT_C, which is adjusted to the heart rate. Nevertheless, in some cases, people suffering from the Long-QT syndrome appear to have a normal QT interval, hence the suggestion to call it congenital repolarization syndrome [18].

People suffering from this pathology show mutated genes which encode either ion-channels or proteins in charge of modifying the function of these channels. These channels are responsible for regulating the flow of sodium, calcium and potassium in cardiac myocytes and, when mutated, cause changes in the mentioned flows [19]. For example, if the outward flow of the potassium current during the 3rd stage of the action potential is decreased or there is late entry of sodium ions in the myocytes due to a defect in the corresponding channels, the APD is enlarged and this leads to a QT prolongation compared to the physiological case [20].

Although the frequency of Long-QT syndrome is still not certainly known, it possibly ranges from 1:2000 to 1:5000 [21] [22] and research on the topic is of great importance due to the fact that the Long-QT Syndrome can lead to sudden death caused by ventricular

upna Universidad Pública de Navarra Nafarroako Unibertsitate Publikoa
Todos los derechos reservados
Eskubide guztiak erresalbatu dira

fibrillation. Episodes may be provoked by various stimuli, depending on the subtype of the condition [17].

3.2 Subtypes

LQTS can arise from mutation of one of several genes [20]. Mutations in the alpha-subunit-regulating genes of three channels are the most common genetic causes for LQTS. Those mentioned three channels are: the slowly activating potassium repolarization channel (KCNQ1; LQT1); the rapidly activating potassium repolarization channel (KCNH2; LQT2) and the sodium channel (SCN5A; LQT3). In the first two cases the I_{Ks} and I_{Kr} appear reduced, whereas the third one shows an increase in late I_{Na} flow. In addition, LQTS has been identified in patients with mutations involving the auxiliary beta-subunits of KCNQ1 (minK; LQT5) and of KCNH2 (MiRP1; LQT6). Furthermore, until this day a high number of mutations in channel and proteins have been found and registered, fact that has led to a classification of LQTS in at least ten subtypes. However, it's imperative to keep in mind that mutations in these same channels may cause other disease phenotypes [17].

As mentioned, LQTS can be classified in at least 10 subtypes, depending on the mutated gene or the mutation type. Nevertheless this work will focus on Long-QT Syndromes 1, 2 and 3 for being the most common. In these subtypes, the genes encoding the subunits of the proteins forming the currents I_{Ks}, I_{Kr}, and I_{Na} are mutant, respectively.

Table 3.1. Brief description of the main subtypes of the Long-QT Syndrome. Adapted from [19]

Subtype	Frequency	Gene	Ion Channel Deffect
LQT-1	30-35%	KCNQ1	alpha subunit of slowly activating delayed rectifier K+ channel
LQT-2	25-30%	HERG	alpha subunit of rapidly activating delayed rectifier K+ channel
LQT-3	5-10%	SCN5A	alpha subunit of voltage gated Na+ channel
LQT-4	1-2%	ANKB	Ankyrin B adaptor protein that anchors Na+-K+ ATPaseand Na+/Ca2+ exchanger
LQT-5	1%	Mink (KCNE1)	beta subunit of slowly activating delayed rectifier K+ channel

3.2.1 Long-QT Type 1

LQT1 is the most common type of Long-QT syndrome, occurring in a 30 percent of all cases approximately. It is caused by mutations in the α - subunit of the Kv7.1 channel

upna Universidad Pública de Navarra Nafarroako Unibertsitate Publikoa
Todos los derechos reservados
Eskubide guztiak erresalbatu dira

protein. Kv7.1 is a potassium channel protein coded for by the gene KCNQ1, which has been isolated to chromosome 11p15.5 [23]. The channel is responsible for the slowly deactivating delayed rectifier potassium current I_{Ks}. Mutations in this gene mainly cause a decrease on the flow of I_{Ks} which leads to transmural dispersion of repolarization in the left ventricular wall [17]. When dysfunctional I_{Ks}, outstanding $I_{Ca,L}$ causes a delayed repolarization. The APD of all cell types is enlarged, due to the fact that I_{Kr} is nearly homogeneously distributed throughout the heart [6]

The function of KCNQ1 was defined thanks to studies performed by Sanguinetti et al. [24] and Barhanin et al. [25]. They used Chinese hamster ovary cells and COS cells to find that cotransfection with KCNE1 was required to form the I_{Ks} current. Melman et al. [26] demonstrated that all KCNE-binding sites of Kv7.1 are required for proper regulation by the accessory subunit. [20].

3.2.2 Long-QT Type 2

LQT2 appears less frequently than LQT1, being the second most common among all the Long-QT Syndromes. It is found in approximately 25 percent of the cases. It also affects the potassium channel but the affected gene is the so called human ether-a-go-go related gene (hERG), which is responsible for the potassium rapid rectifying current, I_{Kr}, whereas the affected current in LQT1 was I_{Ks}. As well as I_{Ks}, I_{Kr} influences the termination of the cardiac action potential and its flow keeps the heart from early after depolarizations. The LQT2 related mutations reduce the current, thus K ions find it more difficult to pass through. The remaining repolarizing current I_{Ks} is heterogeneously distributed, hence the more significant prolongation of the APD in M cells, rather than Endo and Epi cells.

3.2.3 Long-QT Type 3

Although less common than the first two types, LQT3 is more lethal than the above described. Unlike for LQT1 and LQT2 the affected channel here is not a potassium channel but a sodium one. The current named I_{Na} flows through the channel and is responsible for the fast upstroke of the AP. A defect in gene SCN5A keeps the channel from remaining inactivated, causing late flow of I_{Na}, fact that does not happen in physiological cases. Therefore, APD is enlarged. The effect is noticeable in all cell types, although more significant in M cells, due to the already longer Plateau phase.

3.3 Diagnosis

Cardiologists usually receive potential Long-QT patients after they experience a cardiac arrhythmia, syncope, an aborted cardiac arrest, episode of palpitation, or sudden

upna Universidad Pública de Navarra Nafarroako Unibertsitate Publikoa
Todos los derechos reservados
Eskubide guztiak erresalbatu dira

death/cardiac arrest in a relative. Usually, a differential diagnosis is performed which includes hypertrophic cardiomyopathy (HCM), arrhythmogenic right ventricular cardiomyopathy/dysplasia (ARVC/D), long QT syndrome, drug-induced QT prolongation, Brugada syndrome (BS), and some other even less frequent causes of sudden death in young age groups [16].

A detailed family history is imperative since it looks for a history of syncope or sudden unexplained death not only in first-degree relatives but also in more remote relatives in the family [27]. ECGs are obtained not only from the patient but from direct relatives as well, with the purpose of identifying enlarged QT intervals or irregular T-wave shapes. As mentioned, not all patients suffering from Long-QT have a long QT interval on an ECG; the QT interval may change from time to time [28]. In patients with normal QT_C, abnormal T-wave morphology may provide useful information, hence the importance to perform multiple ECGs and careful evaluations of T-wave morphology in these ECGs [16].

Physical exams looking for signs of conditions that may lower blood levels of potassium or sodium are also performed. These conditions include the eating disorders anorexia nervosa and bulimia, excess vomiting or diarrhea, and certain thyroid disorders [28].

3.3.1 Long-QT Score

In 1993, Schwartz and colleagues [29] published a diagnosis score which proposes that if a value of at least 4 is reached, the probability of Long-QT diagnosis is high whereas in the case of score values of 2 to 3, the plausibility of diagnosis is lower. This method is shown in figure 3.1. What's remarkable about this score is the fact that it's not only based on the QT interval but it also relies on findings frequently seen in Long-QT patients, such as T-wave alternans, T-wave notches or bradycardia [16].

3.3.2 Genetic Testing

The main point where genetic testing is useful is family screening. Identifying the mutation in a proband provides an opportunity to conduct genotyping of family members who frequently cannot be diagnosed just based on ECG data [27]. Besides, the clinical course is different by genotype, [30], [31] and the treatment differs depending on the Long-QT subtype, thus genetic testing is an important diagnosis procedure. However, this method is limited by its excessively high cost and its lack of accuracy; about one-third of LQTS cases cannot be detected by these tests and as many as one-third of the people who test positive for LQTS don't have any signs or symptoms of the disorder [32].

upna Universidad Pública de Navarra Nafarroako Unibertsitate Publikoa
Todos los derechos reservados
Eskubide guztiak erresalbatu dira

Table 2. Clinical diagnostic criteria for LQTS*

Electrocardiogram Findings†	Points
Corrected QT interval, seconds	
≥0.48	3
0.46-0.47	2
0.45 (in males)	1
Torsades de pointes‡	2
T-wave alternans	1
Notched T wave in 3 leads	1
Low heart rate for ages§	0.5
Clinical history	
Syncope‡	
With stress	2
Without stress	1
Congenital deafness	0.5
Family history▒	
Family members with definite LQTS	1
Unexplained sudden cardiac death at under 30 years among immediate family member(s)	0.5

* Reprinted from Schwartz et al. *Circulation 1993,88:782-4.* Scoring: ≤1 point, low probability of LQTS; 2 to 3 points, intermediate probability of LQTS; and ≥4 points, high probability of LQTS.

† Findings in the absence of medications or disorders known to affect these electrocardiogram findings. The corrected QT interval (QTc) is calculated by the Bazett formula: $QTc = QT/\sqrt{RR}$, where R-R is the time interval between 2 consecutive QRS complexes on electrocardiogram.

‡ Torsades de pointes and syncope are mutually exclusive.

§ Resting heart rate below the second percentile for age.

▒ The same family member cannot be counted in both categories

Fig. 3.1. Long-QT diagnosing score. Taken from [27]

upna Universidad Pública de Navarra Nafarroako Unibertsitate Publikoa
Todos los derechos reservados
Eskubide guztiak erresalbatu dira

upna Universidad Pública de Navarra Nafarroako Unibertsitate Publikoa
Todos los derechos reservados
Eskubide guztiak erresalbatu dira

4

Methods

4.1 Data Acquisition

4.1.1 Voltage Clamp Technique

The voltage clamp technique is an electrophysiological method for measuring ion currents across the membrane of excitable cells while holding the membrane voltage at a set level. The voltage clamp allows the membrane voltage to be manipulated independently of the ionic currents, allowing the current-voltage relationships of membrane channels to be studied.

This procedure was first introduced by Kenneth Cole and George Marmount in 1949 and after experiments with the voltage clamp, Alan Hodgkin and Andrew Huxley outlined the ionic causes of the action potential in 1952.

The voltage clamp apparatus consists of a feedback amplifier, a voltage amplifier, and an ammeter. The voltage amplifier is connected to a voltage electrode inserted inside the cell, and to the feedback amplifier. The feedback amplifier is connected to a current electrode. Finally, a ground electrode completes the feedback and voltage circuits through an ammeter to ground.

During the performance of the technique, the researcher sets the holding voltage, called command voltage V_c, and the voltage amplifier measures V_m. A comparator determines the difference between V_c and V_m and generates a difference signal if both voltages are not equal. This signal is sent to the feedback amplifier, which sends an output to the current electrode and current is injected into the cell in order to make V_c equal to V_m. Thus, the clamp circuit produces a current equal and opposite to the ionic currents flowing across the cell membrane, which can easily be measured using the ammeter.

upna Universidad Pública de Navarra Nafarroako Unibertsitate Publikoa
Todos los derechos reservados
Eskubide guztiak erresalbatu dira

Figure 4.1 shows an example of a voltage clamp protocol. The membrane voltage is stepped from resting potential to different voltages which are held (holding voltage) a certain amount of time that can vary according to the experiment. During this time, current flowing across the membrane is measured, leading to the curves in the image. After the step, the voltage is set back to resting voltage causing what is called tail current to, finally, go back to resting voltage until no current flows.

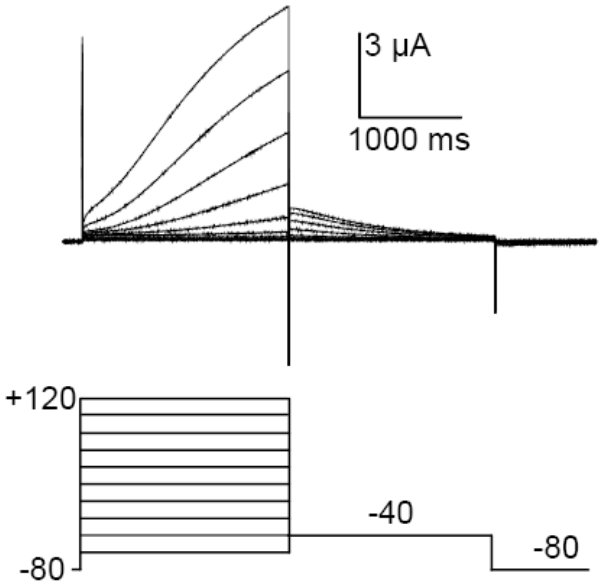

Fig. 4.1. Example of a voltage clamp protocol with both the applied voltages and the measured currents. This data was provided by the university hospital in Heidelberg and will be used for the research in this paper.

4.1.2 Patch Clamp Technique

The patch clamp technique is a refinement of the voltage clamp method and it allows recordings in single ion channel currents. It was first used by Neher and Sakmann (1976) to resolve currents through single acetylcholine-activated channels in cell-attached patches of membrane of frog skeletal muscle [33]. The principle of the method is to electrically isolate a patch of membrane from the external solution and to record current flowing into the patch. That patch contains just one or a few ion channel molecules.

A fire-polished glass pipette, previously filled with a suitable electrolyte solution, is pressed against the surface of a cell and bonds with the cell membrane by a negative pressure present at the tip. A seal whose electrical resistance is more than 10 Gigaohms forms between the edge of the pipette and the patch, and the currents can be recorded. This high seal resistance is needed for two reasons. First, the higher the seal resistance, the

upna Universidad Pública de Navarra Nafarroako Unibertsitate Publikoa
Todos los derechos reservados
Eskubide guztiak erresalbatu dira

more complete is the electrical isolation of the membrane patch. Second, a high seal resistance reduces the current noise of the recording, permitting good time resolution of single channel currents.

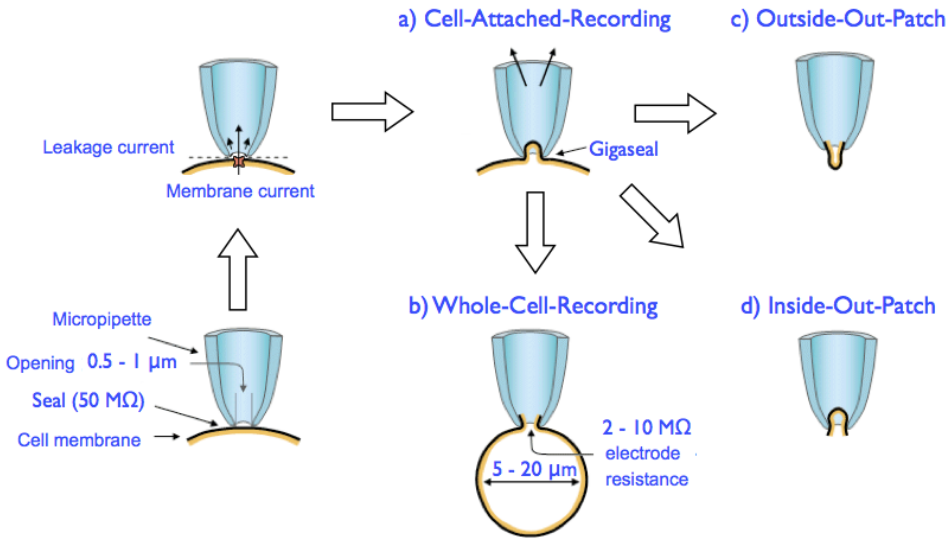

Fig. 4.2. Patch Clamp Technique with miscellaneous configurations. Modified from [34]

Depending on the researchers goals, different variations of the patch clamp technique can be considered. The above explained is the *Cell-attached*, where the electrode is sealed to the patch of membrane, and the cell remains intact. If the investigator wishes to manipulate the environment at the intracellular surface of ion channels, after the gigaseal is formed, the micropipette will be quickly withdrawn from the cell, thus ripping the patch of membrane off the cell. This is called *Inside-Out patch*. It is also possible to perform whole-cell recordings if desired, and that is achieved by the *Whole-Cell-Recording* technique. In this case, the electrode is left in place on the cell, but more suction is applied to rupture the membrane patch, therefore access to the intracellular space of the cell is provided. After application of the Whole-Cell-Recording, the electrode can be slowly withdrawn from the patch. If the electrode is pulled away far enough, the patch will detach from the cell and will reform as a convex membrane at the tip of the pipette. That allows the experimenter to examine the properties of an ion channel when it is isolated from the cell and exposed to different solutions on the extracellular surface of the membrane. Another two variations that can be applied are the *Perforated-Patch* and the *Loose-Patch*, although they're not as widely used as the previous ones.

upna Universidad Pública de Navarra Nafarroako Unibertsitate Publikoa
Todos los derechos reservados
Eskubide guztiak erresalbatu dira

4.1.3 Gathered Data

As described in section 3.2, mutations causing LQT-1 and LQT-2 are responsible for modified kinetics in the potassium ion channels, and, more specifically, they affect the slow and rapid delayed currents. For this work, data was gathered from different sources.

4.1.3.1 LQT-1 Data

The Department of Internal Medicine, University Hospital in Heidelberg gathered the data regarding Long-QT Syndrome 1. LQT-1 related mutation S277L was induced in the KCNQ1 gene and I_{Ks} was recorded for both the wild type and the coexpression of the wild type and the mutation, using the techniques described in 4.1. The exact conditions in which the measurements were performed can be found in [35]. Note how I_{Ks} is indeed reduced for the coexpression case.

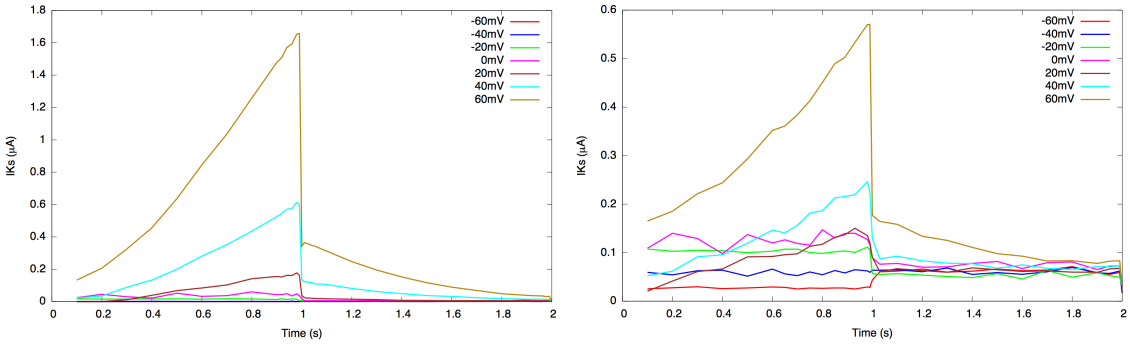

Fig. 4.3. Current-Voltage graphs for I_{Ks} Wild Type (left) and coexpressed S277L mutation (right) characteristics. Different colors express different voltage clamp steps.

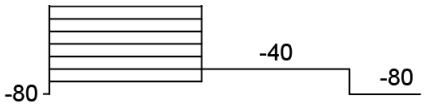

Fig. 4.4. Voltage clamp protocol for LQT-1 measurements. Voltage is applied in 20mV steps, starting at -60mV and ending at 60mV followed by a poststep voltage of -40mV

4.1.3.2 LQT-2 Data

Measurements regarding LQT-2 data were found in [36]. The Experimental and Molecular Cardiology Group and the Departments of Physiology and Clinical Genetics in the University of Amsterdam recorded HERG current, I_{HERG}, on wild-type and type 2 Long-QT syndrome-associated mutant R56Q. These measurements were performed using the

upna Universidad Pública de Navarra Nafarroako Unibertsitate Publikoa
Todos los derechos reservados
Eskubide guztiak erresalbatu dira

techniques mentioned in 4.1, where the values of the ion channel currents were recorded for several transmembrane voltage values. The exact conditions in which the procedure was carried out can be found in [36]

.

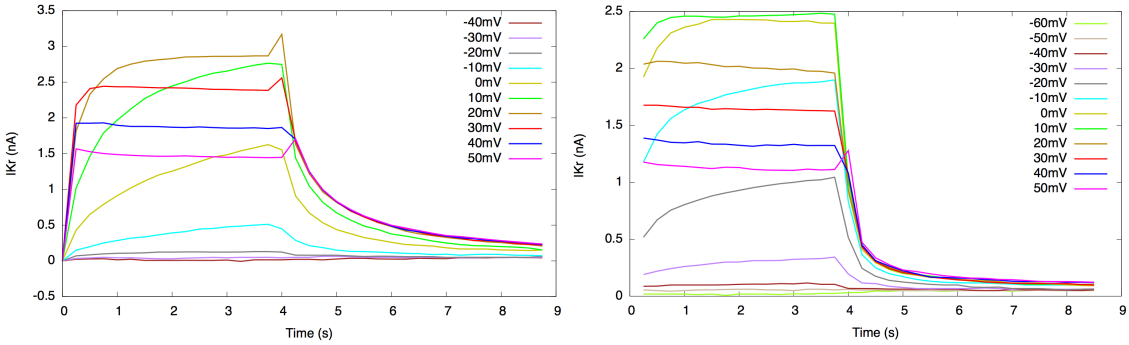

Fig. 4.5. Current-Voltage graphs for I_{HERG} Wild Type (left) and coexpressed R56Q mutation (right) characteristics. Different colors express different voltage clamp steps.

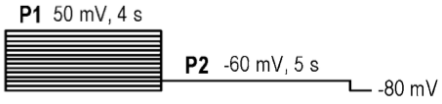

Fig. 4.6. Two step voltage clamp protocol for LQT-2 measurements.

By looking at both the measurement protocol and the voltage-current graphs, P1, is responsible for the activation of the current. I_{HERG} sequentially increases and then decreases in a response to the applied voltages. The second step, P2, stimulates the tail currents in which the top value is a consequence of fast recovery from inactivation, whereas the following decrease is due to deactivation.

4.2 Modelling Cardiac Electrophysiology

The possibilities for doing experimental and clinical studies involving human hearts are very limited. Furthermore, animal hearts used for experimental studies may differ significantly from human hearts, hence the requirement to develop computational models that can help investigating human cardiophysiology.

Mathematical models of cardiac electrophysiology can illustrate the flow of ions into and out of a cell or even the compartments within a cell, and can provide large amounts of information not only about the ion channels themselves, but also about the interaction between these channels and the electrical waves they produce.

upna Universidad Pública de Navarra Nafarroako Unibertsitate Publikoa
Todos los derechos reservados
Eskubide guztiak erresalbatu dira

4.2.1 Ten Tusscher et al. Model

K. H. W. J., Ten Tusscher, D. Noble, P. J. Noble, and A. V. Panfilov formulated a model for human ventricular cells that is based on recent experimental data and that is efficient for large-scale spatial simulations of reentrant phenomena.

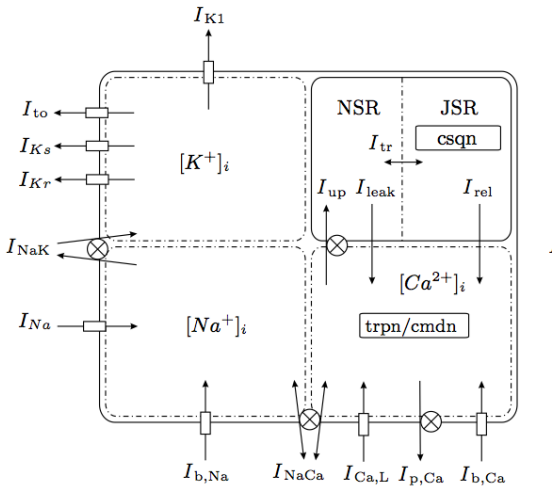

Fig. 4.7. Schematic description of the Ten Tusscher Model. From [6]

The cell membrane is modeled as a capacitor connected in parallel with variable resistances and batteries representing the different ionic currents and pumps and the Nernst potential. The electrophysiological behavior of a single cell can thus be described with the following differential equation

$$\frac{dV_m}{dt} = -\frac{I_{ion} + I_{stim}}{C_m} \tag{4.1}$$

where V is voltage, t is time, I_{ion} is the sum of all transmembrane ionic currents, I_{stim} is the externally applied stimulus and C_m is cell capacitance per unit surface area [37].
The set of transmembrane currents is given by

$$I_{ion} = I_{Na} + I_{K1} + I_{to} + I_{Kr} + I_{Ks} + I_{CaL} + I_{NaCa} + I_{NaK} + I_{pCa} + I_{pK} + I_{bCa} + I_{bK} \tag{4.2}$$

where I_{NaCa} is Na+/Ca2+ exchanger current, I_{NaK} is Na+/K+ pump current, I_{pCa} and I_{pK} are plateau Ca2+ and K+ currents, and I_{bCa} and I_{bK} are background Ca2+ and K+ currents [37].

upna Universidad Pública de Navarra Nafarroako Unibertsitate Publikoa
Todos los derechos reservados
Eskubide guztiak erresalbatu dira

For this work, however, we will focus on the slow and rapid delayed potassium currents and the sodium current, being them the ones affected by the mutations in the first three LongQT syndromes. These currents were described by Ten Tusscher *et al.* via the following expressions.

Slow Delayed Rectifier Current

$$I_{Ks} = G_{Ks} x_s^2 (V - E_{Ks}) \tag{4.3}$$

$$x_{s,\infty} = \frac{1}{1 + e^{(-5-V)/14}} \tag{4.4}$$

$$\alpha_{xs} = \frac{1400}{\sqrt{1 + e^{(5-V)/6}}} \tag{4.5}$$

$$\beta_{xs} = \frac{1}{1 + e^{(V-35)/15}} \tag{4.6}$$

$$\tau_{s,\infty} = \alpha_{xs}\beta_{xs} + 80 \tag{4.7}$$

x_s is an activation gate with α_{xs} and β_{xs} its correspondent transition rates. E_{Ks} represents a reversal potential determined by a large permeability to potassium and a small permeability to sodium and $x_{s,\infty}$ and $\tau_{s,\infty}$ stand for steady state activation curve and activation steady state time constant respectively. For further information see [37] and [38].

Rapid Delayed Rectifier Current

$$I_{Kr} = G_{Ks}\sqrt{\frac{K_o}{5.4}} x_{r1} x_{r2} (V - E_K) \tag{4.8}$$

$$x_{r1,\infty} = \frac{1}{1 + e^{(-26-V)/7}} \tag{4.9}$$

$$\alpha_{xr1} = \frac{450}{1 + e^{(-45-V)/10}} \tag{4.10}$$

$$\beta_{xr1} = \frac{6}{1 + e^{(V+30)/11.5}} \tag{4.11}$$

$$x_{r2,\infty} = \frac{1}{1 + e^{(V+88)/24}} \tag{4.12}$$

upna Universidad Pública de Navarra Nafarroako Unibertsitate Publikoa
Todos los derechos reservados
Eskubide guztiak erresalbatu dira

$$\alpha_{xr2} = \frac{3}{1 + e^{(-60-V)/20}} \tag{4.13}$$

$$\beta_{xr2} = \frac{1.12}{1 + e^{(V-60)/20}} \tag{4.14}$$

x_{r1} and x_{r2} are activation and inactivation gates respectively, with α_{xr1}, β_{xr1}, α_{xr2} and β_{xr2} their correspondent transition rates. $x_{r1,\infty}$ and $x_{r2,\infty}$ stand for steady state activation and inactivation curves.

An exhaustive description of the currents and constants can be found in [38].

4.2.2 Adjustment of Simulation Data to Measurements

The Script Optimizer of the Institute Of Biomedical Engineering is a tool for fitting functions or cell models to a set of measurement points by modifying variable parameters of the function/model. In every iteration step the ScriptOptimizer compares the difference of the measurement points and the simulated curves and tries to adjust the variable parameters. These iterations are performed till the sum of the fitness values reaches a minimum.

In the present case, the objective was to construct models for myocytes affected by LQT-1 and LQT-2 related mutations respectively, by integrating them in the Ten Tusscher cell model. Thus, some parameters and constants in the Ten Tusscher equations for both I_{Ks} and I_{Kr} were chosen and their values were optimized using the Script Optimizer, in order to adjust kinetics of ionic currents to our sets of measurements. Simulations were carried out for wild type cases and both LQT-1 and LQT-2 mutations and the optimized parameters can be seen in tables 4.1 and 4.2.

4.2.2.1 Integration of LongQT-1 in the Model

The data presented in section 4.1.3.1 was used to construct the LQT-1 related model. With the purpose of integrating the channel kinetics, a two-step optimization was required. It is important to keep in mind that parameters regarding temperature and ionic distribution had to be adjusted in the original Ten Tusscher model (i.e the initial values of the K, Na and Ca concentrations), so that the simulation conditions resembled the actual conditions present at time of the measurement experiments.

The first step of the process covered the optimization of the slow-delayed conductance, g_{Ks}, and the temperature correcting factor K_{Q10_Xs}, to fit the Wild Type data. This way, a better approximation to the control data would be achieved and the base would be settled

upna Universidad Pública de Navarra Nafarroako Unibertsitate Publikoa
Todos los derechos reservados
Eskubide guztiak erresalbatu dira

to get a better approach to the data regarding the mutation, which would be the second step of the process. The idea, *a priori*, was to set the new values for these two parameters and then fit the data with the coexpression of the wild type and the mutation by just changing parameters linked to the steady-state curve of the activation gate, the transition rates and the time constant. However, *a posteriori* and after several trials, results showed that it was necessary to include g_{Ks} in the second step and optimize it again. These first results also revealed that not all the values present in the Ten Tusscher equations needed to be changed.

Table 4.1. Brief description of the parameters regarding I_{Ks} to be optimized by Script Optimizer

Parameter	**Description**	**Original value**
g_Ks	I_{Ks} conductance	0.392
K_Q10_Xs	Temperature correcting factor for the activation gate x_s	1
m_Xs_1	Constant in the equation for the steady state activation curve $x_{s,\infty}$	-5
m_Xs_2	Constant in the equation for the steady state activation curve $x_{s,\infty}$	14
a_Xs_1	Constant in the equation for α_{xs}	5
a_Xs_2	Constant in the equation for α_{xs}	6
b_Xs_1	Constant in the equation for β_{xs}	-35
b_Xs_1	Constant in the equation for β_{xs}	15
tau_Xs	Constant in the equation for $\tau_{s,\infty}$	80

4.2.2.2 Integration of LongQT-2 in the Model

For the construction of the LQT-2 related model, data presented in section 4.1.3.2 was used. Just like in the previous case, a two-step optimization was required and parameters regarding temperature and ionic distribution had to be adjusted in the original Ten Tusscher model. However, unlike for LQT-1, the first step of the process not only covered the optimization of the rapid-delayed conductance, g_{Kr}, and the temperature correcting factor $K_{Q10\_Xr,1}$, ($K_{Q10\_Xr,1}$ remained with the original value) but also the constants in the steady state activation and inactivation curves needed to be included to perform the adjustment to the wild type data. All these parameters were included again for the adjustment to the coexpressed data together with constants in the transition rates. Once again, several trials revealed that not all the values needed to be changed.

upna Universidad Pública de Navarra Nafarroako Unibertsitate Publikoa
Todos los derechos reservados
Eskubide guztiak erresalbatu dira

Table 4.2. Brief description of the parameters regarding I_{Kr} to be optimized by Script Optimizer

Parameter	**Description**	**Original value**
g_Kr	I_{Kr} conductance	0.153
K_Q10_Xr_1	Temperature correcting factor for the activation gate x_{r1}	1
K_Q10_Xr_2	Temperature correcting factor for the inactivation gate x_{r2}	1
m_Xs_1_1	Constant in the equation for the steady state activation curve $x_{r1,\infty}$	-26
m_Xs_1_2	Constant in the equation for the steady state activation curve $x_{r1,\infty}$	7
m_Xs_2_1	Constant in the equation for the steady state inactivation curve $x_{r2,\infty}$	-88
m_Xs_2_1	Constant in the equation for the steady state inactivation curve $x_{r2,\infty}$	24
a_Xs_1_1	Constant in the equation for α_{xr1}	-45
a_Xs_1_2	Constant in the equation for α_{xr1}	10
a_Xs_2_1	Constant in the equation for α_{xr2}	-60
a_Xs_2_2	Constant in the equation for α_{xr2}	20
b_Xs_1_1	Constant in the equation for β_{xr1}	-30
b_Xs_1_2	Constant in the equation for β_{xr1}	11.5
b_Xs_2_1	Constant in the equation for β_{xr2}	60
b_Xs_2_2	Constant in the equation for β_{xr2}	20

upna Universidad Pública de Navarra Nafarroako Unibertsitate Publikoa
Todos los derechos reservados
Eskubide guztiak erresalbatu dira

4.2.3 Clancy and Rudy: Integration of LongQT-3

Unlike for LQT-1 and LQT-2, LQT-3 was integrated in the Ten Tusscher model by using a Markovian chain, based in the Clancy and Rudy method. Clancy and Rudy developed a model describing the physiological and mutant I_{Na} channel with a Markovian chain model.

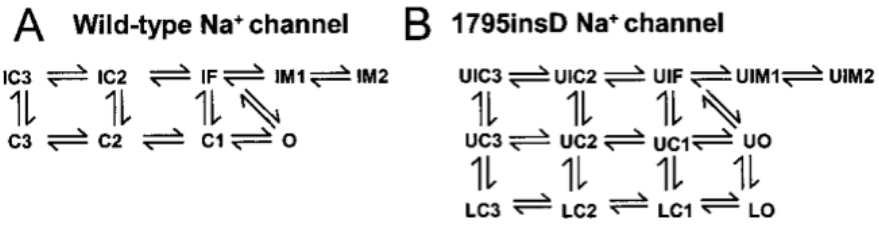

Fig. 4.8. Markovian models for WT (A) and 1795insD (B) cardiac Na channels. Taken from [39]

.

This chain model describes the behavior of the channel and incorporates new features to previously formulated methods. Among those new features new intermediate inactivation states can be found, to more accurately simulate channel inactivation and recovery. IM1 keeps the majority of channels from reopening during depolarization. Two closed-inactivation states IC2 and IC3 are introduced to represent channel availability.

Regarding the model for the mutant channel, it is composed of two modes, the background and the burst. It can be seen that the background mode resembles the wild type, but in this case recovery rates from inactivation are reduced and transitions into UIM1 and UIM2 are faster. The burst mode describes the behavior of the channels that fail to inactivate. Due to these channels, late I_{Na} is generated during the Plateau phase [39].

4.2.4 Tissue Modeling

Cell modeling has been previously described but, in order to resemble the behaviour of a group of cells, simulating the ionic flow outside the cell is of great importance. Tissue models can reconstruct the current flowing through the intra- and extracellular space, and through the gap junctions. The most important models for the propagation of electrical impulses in the cardiac tissue are the bidomain and monodomain models.

4.2.4.1 Bidomain Model

The bidomain model describes the intra- and extracellular space as two domains separated by the cell membrane. Conductivity tensors for each domain are integrated, which considers the anisotropic electrical properties of the tissue, which are different in each of

upna Universidad Pública de Navarra Nafarroako Unibertsitate Publikoa
Todos los derechos reservados
Eskubide guztiak erresalbatu dira

the spaces (fiber orientation dependent outside the cell and gap junction density dependent inside of it). Thus, anisotropy can vary from cell to cell. The distribution of electric potentials can be described for each domain with the Poisson's equation for stationary electrical field as follows:

$$\nabla(\sigma_e \nabla \Phi_e) = -\beta I_m - I_{se} \tag{4.15}$$

$$\nabla(\sigma_i \nabla \Phi_i) = \beta I_m - I_{si} \tag{4.16}$$

where Φ_i and Φ_e are the intra- and extracellular potentials, respectively, σ_i and σ_e the corresponding volume-averaged conductivity tensors, I_m the transmembrane current density, β the surface to volume ratio of the cell, and I_{si} and I_{se} an externally applied current.

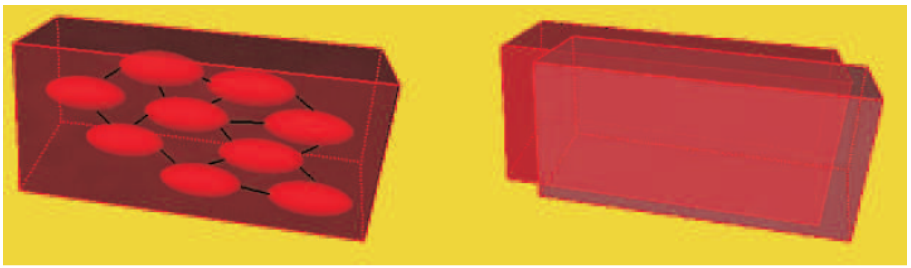

Fig. 4.9. The two domains of the bidomain model. The intracellular space is separated from the extracellular space by a membrane. Adapted from [40]

.

Conductivity tensors represent the conductivities in longitudinal $\sigma_{(e,i)l}$ and transversal $\sigma_{(e,i)t}$ directions of the fiber. The orientation of the main axis of the fiber in the global coordinate system is expressed by the rotation matrix R

$$\sigma_{(e,i)global} = R \begin{pmatrix} \sigma_{(e,i)l} & 0 & 0 \\ 0 & \sigma_{(e,i)t} & 0 \\ 0 & 0 & \sigma_{(e,i)t} \end{pmatrix} R^T \tag{4.17}$$

The rotation matrix is conducted of two components R_{xy} and R_{xz}, whereas R equals $R_{xy}R_{xz}$:

upna Universidad Pública de Navarra Nafarroako Unibertsitate Publikoa
Todos los derechos reservados
Eskubide guztiak erresalbatu dira

$$R_{xy} = \begin{pmatrix} \cos\psi & \sin\psi & 0 \\ -\sin\psi & \cos\psi & 0 \\ 0 & 0 & 1 \end{pmatrix} \tag{4.18}$$

$$R_{xz} = \begin{pmatrix} \cos\theta & 0 & \sin\theta \\ 0 & 1 & 0 \\ -\sin\theta & 0 & \cos\theta \end{pmatrix} \tag{4.19}$$

ϕ describes the angle of the fibre orientation in the (x,y)-plane and θ describes the angle of the fibre orientation in the (x,z)-plane. The transmembrane voltage can be calculated as follows:

$$V_m = \Phi_i - \Phi_e \tag{4.20}$$

Summing the previous Poisson's equations we reach the following

$$\nabla(\sigma_i \nabla \Phi_i) = -\nabla(\sigma_e \nabla \Phi_e) \tag{4.21}$$

$$\nabla(\sigma_i \nabla(V_m + \Phi_e)) = -\nabla(\sigma_e \nabla \Phi_e) \tag{4.22}$$

$$\nabla(\sigma_i \nabla V_m) + \nabla(\sigma_i \nabla \Phi_e) = -\nabla(\sigma_e \nabla \Phi_e) \tag{4.23}$$

$$\nabla((\sigma_i + \sigma_e) \nabla \Phi_e) = -\nabla(\sigma_i \nabla V_m) \tag{4.24}$$

This first bidomain equation describes the effect of the transmembrane voltage on the extracellular potential. For the second bidomain equation, Poisson equation 4.15 can be rewritten using 4.20 leading to:

$$\nabla(\sigma_i \nabla \Phi_i) = \nabla(\sigma_i \nabla(V_m + \Phi_e)) = \nabla(\sigma_i \nabla V_m) + \nabla(\sigma_i \nabla \Phi_e) = -\beta I_m - I_{si} \tag{4.25}$$

According to Hodgkin and Huxley [41], I_m can be described as

$$I_m = \beta_m (C_m \frac{dV_m}{dt} + I_{mem}) \tag{4.26}$$

and combining that with the previous findings, we reach to the second bidomain equation:

$$\nabla(\sigma_i \nabla V_m) + \nabla(\sigma_i \nabla \Phi_e) = \beta (C_m \frac{dV_m}{dt} + I_{mem}) - I_{si} \tag{4.27}$$

4.2.4.2 Monodomain Model

The monodomain model is just a simplified version of the just explained bidomain model. In this case, the anisotropy ratio will be considered equal in both sides of the cell, and thus the conductivities will only differ in a constant scalar ($\sigma_e = k\sigma_i$). Therefore, the resulting equation will be the following:

upna Universidad Pública de Navarra Nafarroako Unibertsitate Publikoa
Todos los derechos reservados
Eskubide guztiak erresalbatu dira

$$\nabla(\sigma_i \nabla V_m) = -((\sigma_i + \frac{\sigma_i}{k})\nabla \Phi_e) = -(1+\frac{1}{k})\nabla(\sigma_i \nabla \Phi e) = (k+1)\beta(C_m \frac{dV_m}{dt} + I_{mem}) \quad (4.28)$$

4.2.5 Anatomical Modeling

Magnetic resonance images were used to build the anatomical models of the ventricles and the torso. With the purpose of conducting the forward calculations, the voxels in the torso model were converted to tetrahedrons and the node-density of the resulting mesh was higher in the heart than anywhere else. More information can be found in [42].

4.2.6 Forward Calculation of the ECG

Different transmembrane voltage distributions were obtained from each of the various heterogeneous electrophysiological configurations explained in section 4.3. After interpolating these distributions onto the anatomical model described above, extracellular potentials were determined by applying the bidomain equations. Details on this procedure can be found in [43].

At the same positions that were used for the multichannel ECG recording (see section 4.3.2) we extracted body surface potentials. The position of the electrodes and a visualization of the thoracic model can be found in [42].

4.3 Adjustment of the T-wave

It is commonly accepted that the associated dispersion of repolarization (DOR) is mainly responsible for the shape of the T-Wave, although its concordance and exact morphology remain not completely understood. DOR is due to differences in action potential duration in myocytes from different regions of the heart and in human cardiac myocytes the slowly delayed rectifier current I_{Ks} is believed to be mainly responsible for these regional differences [44]. In this work, the density of I_{Ks} was varied and heterogeneously distributed in different ways throughout the ventricles, creating different types of DOR. Activation and repolarization of the different heterogeneous I_{Ks} distribution models were calculated using the Ten Tusscher model, and body surface ECGs were simulated and compared to multichannel ECG data in an effort to evaluate the realism of the calculated ECGs.

4.3.1 Electrophysiological Heterogeneities

In order to construct the different configurations of heterogeneous I_{Ks} densities, previous data regarding the topic was gathered from [45] and, based on it, 22 different setups were created. The heterogeneously distributed parameter (g_{Ks}) was stored in a dataset with the

upna Universidad Pública de Navarra Nafarroako Unibertsitate Publikoa
Todos los derechos reservados
Eskubide guztiak erresalbatu dira

same resolution as the anatomical model. Before ventricular activation was initiated, the simulation framework [46] loaded this dataset and replaced g_{Ks} in the electrophysiological model with these values.

4.3.1.1 Transmural Heterogeneities

Concerning the distribution of transmural heterogeneities, many different studies reported a shorter Endo compared to Epi APD [45]. This was considered by reducing the Endo g_{Ks} to 92% of its Epi value according to [47]. All other parameters were taken from the original Ten Tusscher *et al.* publication. Endo, M and Epi cells were arranged in layers of different thicknesses, resulting in the following setup.

- **TM40_30_30:** this setup contained 40% Endo, 30% M and 30% Epi cells. The values of the conductivity for the different cell types were $g_{Ks,Endo}$=0.36064 nS/pF, $g_{Ks,M}$=0.098 nS/pF and $g_{Ks,Epi}$=0.392 nS/pF

4.3.1.2 Apico-Basal Heterogeneities

When it comes to apico-basal APD dispersion, different studies show both larger and smaller APDs in the apex compared to the base. Moreover, the I_{Ks} density was found to be a bit less than twice as large in apical than in basal myocytes [48]. However, [45] showed that the results were better in the case of g_{Ks} being larger at the apex and that a scaling factor of 1.5 wasn't enough. Therefore, due to the fact that the left ventricle mostly consists of Endo cells, [49] this cell type with its specific g_{Ks} value of 0.36064 nS/pF was taken as a basis and different scaling factors were applied to accomplish the gradient. We first chose to model a 2 times larger I_{Ks} density at the apex and then a second model where I_{Ks} was 2.25 times larger at the apex. The values in between were linearly interpolated.

- **A2B1:** Endo g_{Ks} was multiplied by scaling factors from 1 in the base to 2 in the apex. ($g_{Ks,base}$=0.36064 nS/pF , $g_{Ks,apex}$=0.72028 nS/pF)

- **A2.25B1:** Endo g_{Ks} was multiplied by scaling factors from 1 in the base to 2.25 in the apex. ($g_{Ks,base}$=0.36064 nS/pF , $g_{Ks,apex}$=0.81144 nS/pF)

4.3.1.3 Diagonal Heterogeneities

In the previous apico-basal setups the gradient followed a vertical vector starting at the apex and finishing at the base. In order to study if the heterogeneities could be distributed

upna Universidad Pública de Navarra Nafarroako Unibertsitate Publikoa
Todos los derechos reservados
Eskubide guztiak erresalbatu dira

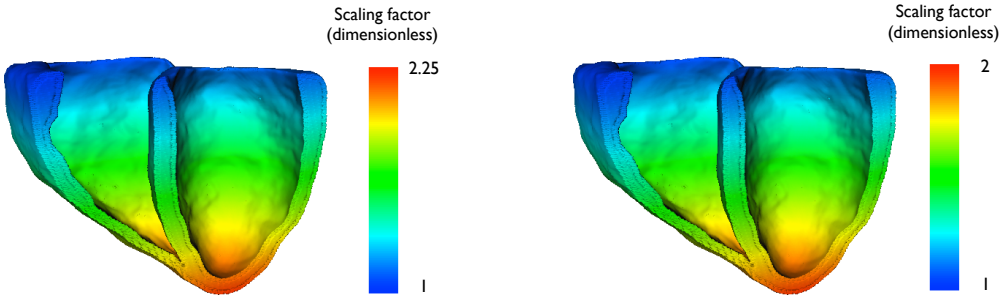

Fig. 4.10. Apico-Basal setups and the corresponding scaling factors

along a different direction we created two configurations in which the gradient followed a diagonal. In the first one, the gradient was set in the direction of the normal vector of a plane that conformed a 45 degree angle with the right ventricle apex. For the second, the plane conformed a 45 degree angle with the left ventricle apex and the gradient followed the direction of the normal vector. The scaling factor was 2 for the starting apex-corner and 1 for the ending base-corner. As in the apico-basal case, Endo cells were chosen for these configurations.

- **A2B1_45deg_RV:** Endo g_{Ks} was multiplied by scaling factors from 1 in the left ventricular base to 2 in the right ventricular apex. ($g_{Ks,Leftbase}$=0.36064 nS/pF , $g_{Ks,Rightapex}$=0.72028 nS/pF)

- **A2B1_45deg_LV:** Endo g_{Ks} was multiplied by scaling factors from 1 in the left ventricular base to 2 in the right ventricular apex. ($g_{Ks,Rightbase}$=0.36064 nS/pF , $g_{Ks,Leftapex}$=0.72028 nS/pF)

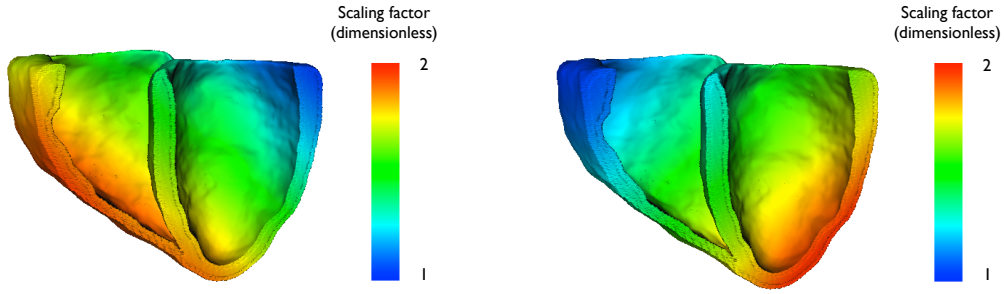

Fig. 4.11. Diagonal setups and the corresponding scaling factors. Note how the gradient follows a diagonal.

upna Universidad Pública de Navarra Nafarroako Unibertsitate Publikoa
Todos los derechos reservados
Eskubide guztiak erresalbatu dira

4.3.1.4 Combination of Apico-Basal and Transmural Heterogeneities

In order to include both apico-basal and transmural gradients at the same time, we multiplied different transmural setups by the scaling factors in the previously mentioned apico-basal configurations. The first transmural setups used for this combinations were chosen based on results in [45] and, from then on, the rest were randomly created by analyzing previous trials. This led to 10 setups:

- **TM40_30_A2B1:** a transmural setup containing 40% of Endo, 30% of M and 30% of Epi cells was multiplied by the scaling factors in A2B1
- **TM40_A2.25B1:** a transmural setup containing 40% of Endo, 30% of M and 30% of Epi cells was multiplied by the scaling factors in A2.25B1
- **TM35_40_A2B1:** a transmural setup containing 35% of Endo, 40% of M and 25% of Epi cells was multiplied by the scaling factors in A2B1
- **TM35_40_A2.25B1:** a transmural setup containing 35% of Endo, 40% of M and 25% of Epi cells was multiplied by the scaling factors in A2.25B1
- **TM35_30_A2B1:** a transmural setup containing 35% of Endo, 30% of M and 35% of Epi cells was multiplied by the scaling factors in A2B1
- **TM35_20_A2.25B1:** a transmural setup containing 35% of Endo, 20% of M and 45% of Epi cells was multiplied by the scaling factors in A2.25B1
- **TM30_30_A2B1:** a transmural setup containing 30% of Endo, 30% of M and 40% of Epi cells was multiplied by the scaling factors in A2B1
- **TM25_40_A2B1:** a transmural setup containing 25% of Endo, 40% of M and 35% of Epi cells was multiplied by the scaling factors in A2B1
- **TM20_15_A2.25B1:** a transmural setup containing 20% of Endo, 15% of M and 65% of Epi cells was multiplied by the scaling factors in A2.25B1
- **TM10_15_A2.25B1:** a transmural setup containing 10% of Endo, 15% of M and 85% of Epi cells was multiplied by the scaling factors in A2.25B1

upna Universidad Pública de Navarra Nafarroako Unibertsitate Publikoa
Todos los derechos reservados
Eskubide guztiak erresalbatu dira

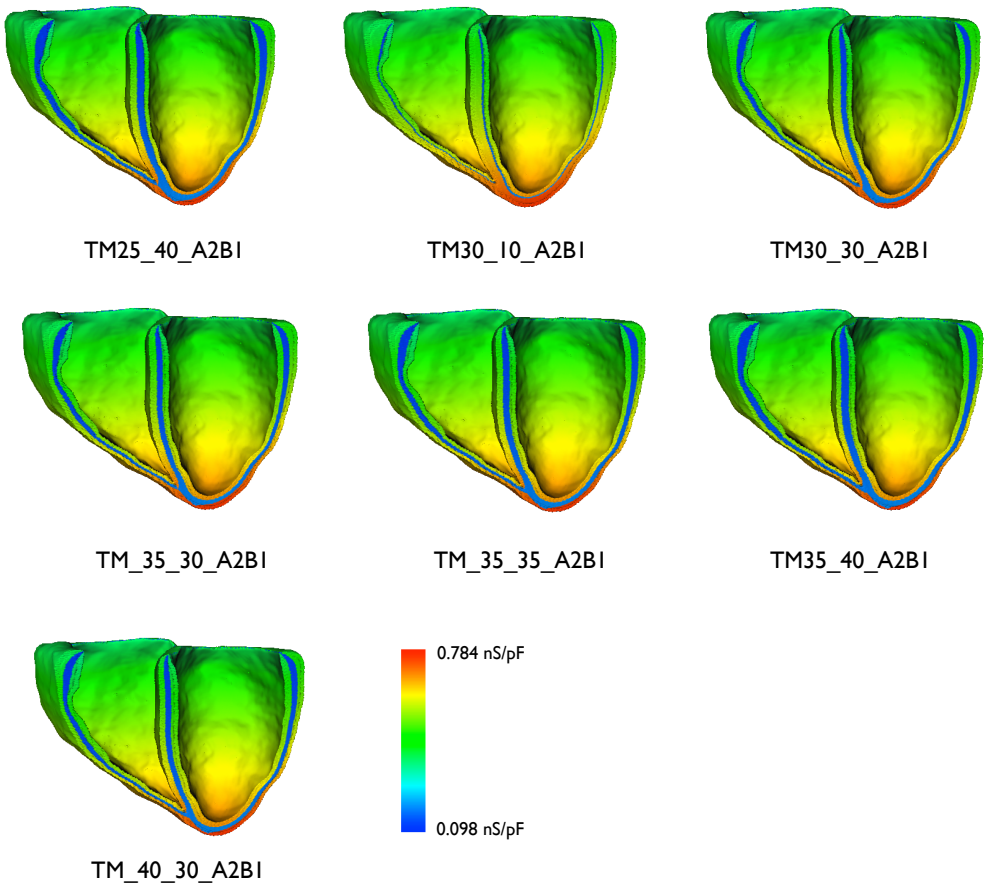

Fig. 4.12. Setups including apico-basal and transmural gradients at the same time

Figure 4.12 shows how by changing the percentages of the different cell types, not only the amount of M cells is changed but also their position. Depending on the setup, M cells appear closer to the endocard or to the epicard and the thickness of the corresponding layer increases or decreases.

4.3.1.5 Reduced g_{Kr}

As explained in the theoretical introduction, both I_{Ks} and I_{Kr} are mainly responsible for the repolarization, specially for the late repolarization. Thus, another option that we considered was to decrease the original value of g_{Kr} in the Ten Tusscher model. Consequently, we first chose setups with an apico-basal gradient and reduced the g_{Kr} to a 50, 20 and 10 percent of the original value. In addition, configurations with combined (apico-basal and transmural) heterogeneities were elected and g_{Kr} was decreased to a 10 percent of its original value.
As a result, 7 configurations were obtained:

upna Universidad Pública de Navarra Nafarroako Unibertsitate Publikoa
Todos los derechos reservados
Eskubide guztiak erresalbatu dira

- **A2B1_50percent:** the original value of g_{Kr} in the A2B1 setup was divided by a factor of 2.

- **A2B1_20percent:** the original value of g_{Kr} in the A2B1 setup was divided by a factor of 5.

- **A2B1_10percent:** the original value of g_{Kr} in the A2B1 setup was divided by a factor of 10.

- **TM30_10_A2B1_10percent:** the original value of g_{Kr} in the combined setup TM30_10_A2B1 was divided by a factor of 10.

- **TM35_35_A2B10percent:** the original value of g_{Kr} in the combined setup TM35_35_A2B1 was divided by a factor of 10.

- **TM40_30_A2.25B10percent:** the original value of g_{Kr} in the combined setup TM40_30_A2.25B1 was divided by a factor of 10.

- **TM40_30_A2B10percent:** the original value of g_{Kr} in the combined setup TM40_30_A2B1 was divided by a factor of 10.

4.3.2 Multichannel ECG Recording

Simulated T-waves needed to be compared to a set of measurements. For this measurements to be performed, a 64-lead system (ActiveTwo, BioSemi, Amsterdam, Netherlands) was used to record multichannel ECG data at 70 beats per minute. The common-mode rejection ratio was increased with the objective of denoising and the reference point was moved to Wilson Central Terminal for the same reason.[50].
116 successive heartbeats were averaged on every channel so that comparison with the simulation results was possible.

4.4 BSPM Simulation

After developing cell models for the Long-QT subtypes and adjusting the T-wave by choosing a setup to model the physiological heterogeneity, Body Surface Potential Maps (BSPM) were simulated all over the thorax for the physiological case and the three subtypes. Nodes were chosen so that the minimum distance among them was 1.7cm leading to 1050 nodes, thus, 1050 signals for each of the cases.

upna Universidad Pública de Navarra Nafarroako Unibertsitate Publikoa
Todos los derechos reservados
Eskubide guztiak erresalbatu dira

upna Universidad Pública de Navarra Nafarroako Unibertsitate Publikoa
Todos los derechos reservados
Eskubide guztiak erresalbatu dira

5

Results

The aim of this work was to analyze the differences in BSPM for each of the first three Long-QT syndromes and try to select electrodes in which those differences were significant. For this purpose, cell models for the syndromes were developed first; more precisely channel kinetics and current reductions were integrated in the Ten Tusscher model as explained in sections 4.2.2.1 and 4.2.2.2. APD was simulated for the physiological case and the three subtypes and restitution functions such as ERP, CV and WL were compared as well. In parallel to those tasks, the physiological heterogeneity in the heart and torso model was adjusted so that the simulated T-wave resembled the measured BSPM. Once the effects of Long-QT 1, 2 and 3 were modeled and the best approach for the T-wave was chosen, BSPM were simulated for the subtypes and, finally, differences between them were evaluated and analyzed not only regarding amplitude but also morphological descriptors for the T-wave. This chapter presents the results obtained in each step of this analysis.

5.1 Parameter Optimization

In order to integrate the effects of LongQT-1 and LongQT-2 in the model, a parameter optimization was performed with the help of the Script Optimizer in which parameters were adjusted to fit both the wild type data and the coexpressed.

5.1.1 LongQT-1

The results for I_{Ks} are shown in figure 5.1. In spite of the fact that the tail current didn't really fit, the results were on the whole satisfactory. Since the current present during the clamp step is more important for cell physiology in general, the main focus was to adjust this current as good as possible which was mainly achieved, although the simulated currents could not reach the peak value of the measurements in some of the cases, especially

upna Universidad Pública de Navarra Nafarroako Unibertsitate Publikoa
Todos los derechos reservados
Eskubide guztiak erresalbatu dira

regarding the wild type data.

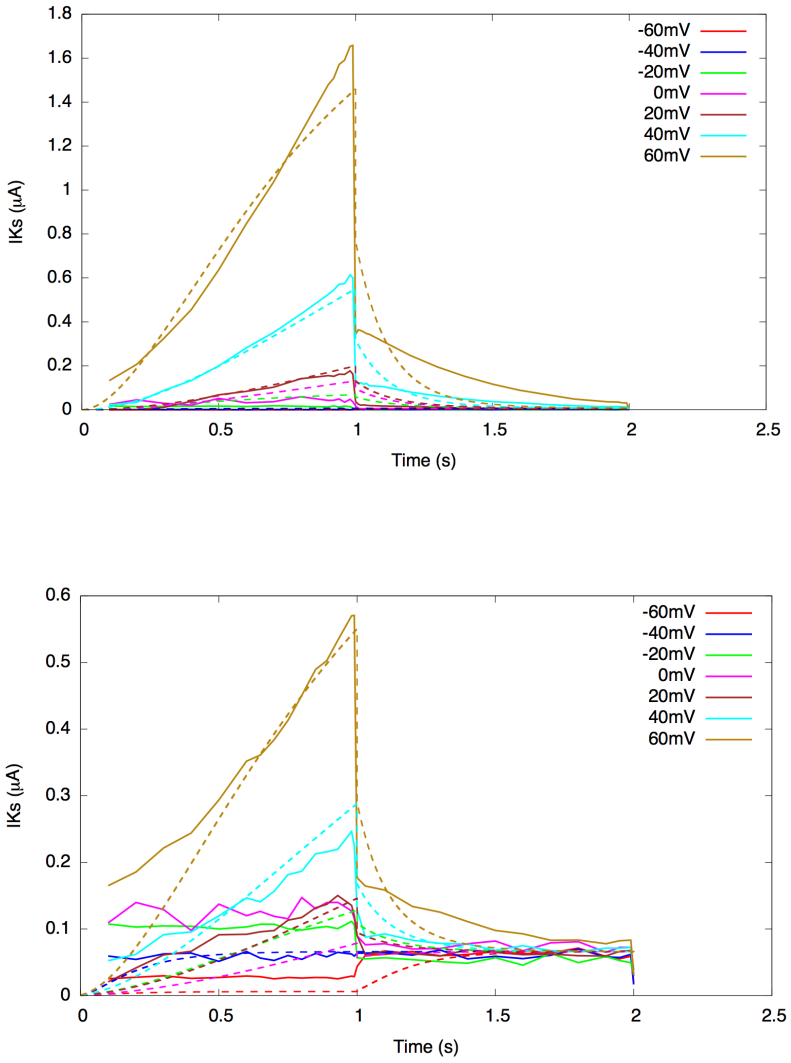

Fig. 5.1. Comparison of simulated current-voltage graphs and measurements for both LQT-1 wild type (top) and coexpressed (bottom) data. Solid lines represent the set of measurements, whereas dashed lines show the results of the simulations.

As explained in section 4.2.2, a two-step optimization was required in which g_{Ks} and K_{Q10} were adapted to the wild type set of measurements and, with the obtained values, an adjustment to the coexpresssed data was performed, in which g_{Ks} was again varied, together with the remaining parameters. In order to construct a model for the subtypes of the LongQT syndrome, the temperature, ionic distribution and K_{Q10} had to be set to the original values. The value of g_{Ks} had to be suited by combining the original value in the Ten Tusscher model and both values obtained in the optimization for the wild type and the coexpressed data. This was made by using the following formula:

upna Universidad Pública de Navarra Nafarroako Unibertsitate Publikoa
Todos los derechos reservados
Eskubide guztiak erresalbatu dira

$$g_{Ks,LQTModel} = \frac{g_{Ks,orig} g_{Ks,Coex}}{g_{Ks,WildType}} \tag{5.1}$$

Table 5.1. Values of the parameters regarding I_{Kr} provided by Script Optimizer and final values used for the Ten Tussher based LQT1 cell model

Parameter	Original value	Adjustment to Wild Type Data	Adjustment to Coexpressed Data	Final Value for the LQT1 Model based on eq. 5.1
g_Ks	0.392	0.01037	0.00422	0.159
K_Q10_Xs	1	1.909	–	1
m_Xs_1	-5	–	-32.8719	-32.8719
m_Xs_2	14	–	–	14
a_Xs_1	5	–	-19.3863	-19.3863
a_Xs_2	6	–	0.2885	0.2885
b_Xs_1	35	–	27.7474	27.7474
b_Xs_2	15	–	22.2581	22.2581
tau_Xs	80	–	–	80

Table 5.1 shows the output values from the Script Optimizer adjustment and the final values used for the Ten Tusscher based LQT-1 cell model, where g_{Ks} was obtained by using the previously mentioned formula. Some of the constants that were initially thought to be included for fitting the coexpressed data were set to the original values after an *a posteriori* analysis of the first trials showed that better approximations to measurements were accomplished this way. Changes in the parameters are quite significant in most of the cases, specially for the conductivity, which presents an expected reduction.

5.1.2 LongQT-2

The results for I_{HERG} are shown in figure 5.2. The sets of measurements for LQT-2 were more complicated to fit and, again, the main focus was to adjust the currents present during the clamp step, hence the lack of resemblance when it comes to tail currents. Just like for the LQT-1 data, simulations couldn't reach the highest current values in some of the cases and tended to stabilize faster than the measured I_{HERG}.

upna Universidad Pública de Navarra Nafarroako Unibertsitate Publikoa
Todos los derechos reservados
Eskubide guztiak erresalbatu dira

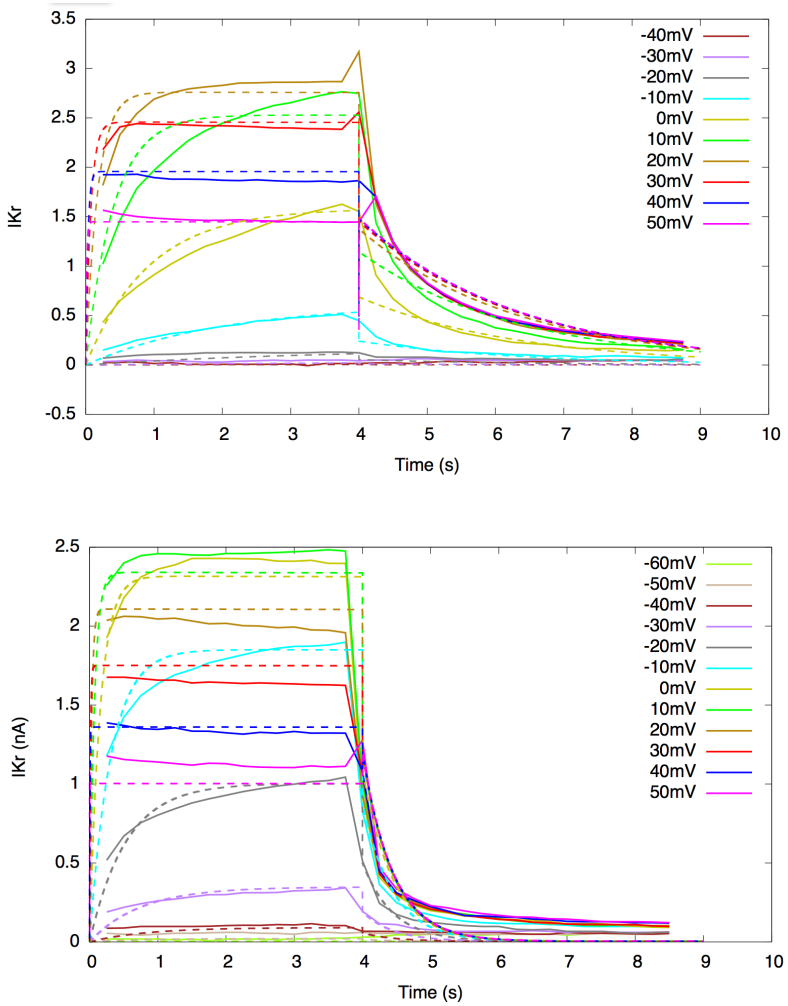

Fig. 5.2. Comparison of simulated current-voltage graphs and measurements for both wild type (top) and LQT-2 coexpressed (bottom) data. Solid lines represent the set of measurements, whereas dashed lines show the results of the simulations.

Unlike for LQT-1, not only g_{Kr} and the temperature correcting factors were adapted to the wild type set of measurements, but the constants present in the equations for the activation and inactivation steady state curves as well. The adjustment to the coexpresssed data included those parameters again together with the remaining. Once again, setting the temperature, ionic distribution and the temperature correcting factors back to the original values was necessary. g_{Kr} was recalculated using equation 5.1 and the constants present in the equations for the activation and inactivation steady state curves were suited by combining the original value in the Ten Tusscher model and both values obtained in the optimization for the wild type and the coexpressed data by using the following formulas:

$$m\_Xr\_i\_1_{LQTModel} = m\_Xr\_i\_1_{orig} - m\_Xr\_i\_1_{WT} + m\_Xr\_i\_1_{Coex} \tag{5.2}$$

upna Universidad Pública de Navarra Nafarroako Unibertsitate Publikoa
Todos los derechos reservados
Eskubide guztiak erresalbatu dira

$$m\_Xr\_i\_2_{LQTModel} = \frac{m\_Xr\_i\_2_{orig} m\_Xr\_i\_1_{Coex}}{m\_Xr\_i\_2_{WT}} \tag{5.3}$$

where i = 1,2

Table 5.2. Values of the parameters regarding I_{Kr} provided by Script Optimizer regarding the LQT2 model.

Parameter	**Original value**	**Adjustment to Wild Type Data**	**Adjustment to Coexpressed Data**	**Final Value for the LQT2 Model based on eqs. 5.2-5.3**
g_Kr	0.153	0.05099	0.04358	0.125
K_Q10_Xr_1	1	5.0457	–	1
K_Q10_Xr_2	1	–	–	1
m_Xr_1_1	-26	0.9362	-17.03	-43.96
m_Xr_1_2	7	7.427	7.694	7.251
m_Xr_2_1	-88	25.324	17.861	-95.463
m_Xr_2_1	24	19.3867	20.984	25.977
a_Xr_1_1	-45	–	-15.7865	-15.7865
a_Xr_1_2	10	–	13.8433	13.8433
a_Xr_2_1	-60	–	55.3022	55.3022
a_Xr_2_2	20	–	–	20
b_Xr_1_1	-30	–	-44.0902	-44.0902
b_Xr_1_2	11.5	–	10.5209	10.5209
b_Xr_2_1	60	–	–	60
b_Xr_2_2	20	–	–	20

Table 5.2 shows the output values from the Script Optimizer adjustment and the final values used for the Ten Tusscher based LQT-2 cell model. Final values for the parameters that were changed for both the adjustment to the wild type data and the adjustment to the coexpressed data were obtained by using the previously mentioned set of equations. As in the optimization for LQT-1 data, some of the constants that were initially thought to be included for fitting the coexpressed data were set to the original values after an *a posteriori* analysis of the first trials showed that better approximations to measurements were accomplished this way. Unlike for LQT-1, the change in the value of the conductivity is not very significant, although we observe an expected reduction. Most of the remaining constants don't experience as meaningful alterations as in the previous case.

upna Universidad Pública de Navarra Nafarroako Unibertsitate Publikoa
Todos los derechos reservados
Eskubide guztiak erresalbatu dira

5.2 Restitution Functions

Once the effects of the three LongQT subtypes were integrated in the Ten Tusscher model, restitution parameters were simulated together with the physiological case. Action potentials for the four cases were obtained and, along with that, the wavelength (WL), conduction velocity (CV) and the effective refractory period (ERP) were also calculated. The wavelenght is the distance travelled within a refractory period, thus, WL defines the shortest path length that is able to sustain reentry and it is described as the product of the CV and the ERP. One cycle of a stimulus is made up of the actual action potential and the period during which a steady state is maintained. This period is called diastolic interval (DI). The sum of APD and DI is the basic cycle length (BCL).

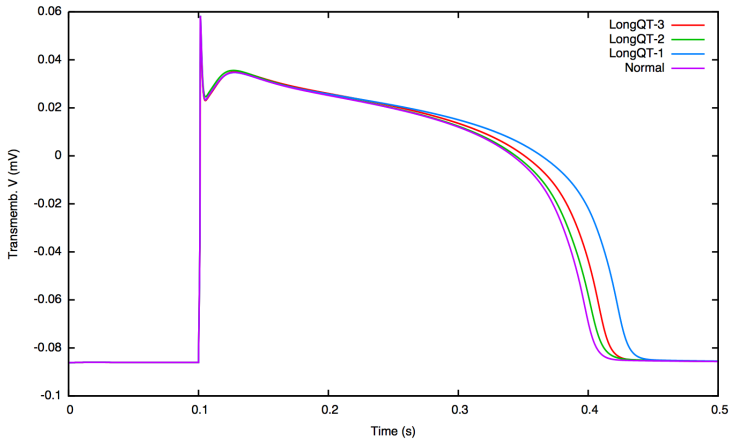

Fig. 5.3. APD for the Long-QT subtypes and the physiological case.

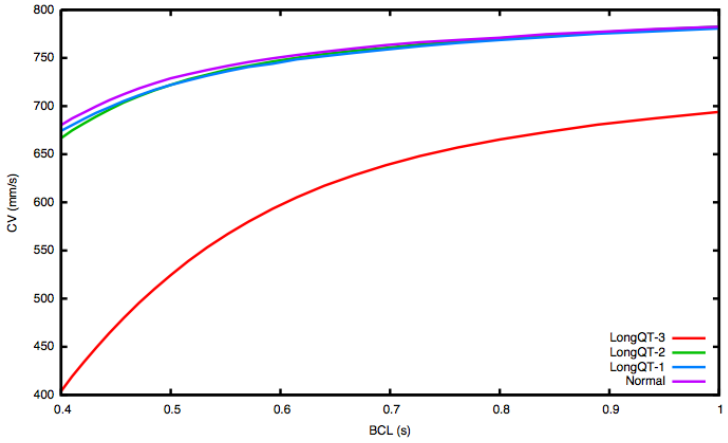

Fig. 5.4. Restitution Functions CV represented against BCL

upna Universidad Pública de Navarra Nafarroako Unibertsitate Publikoa
Todos los derechos reservados
Eskubide guztiak erresalbatu dira

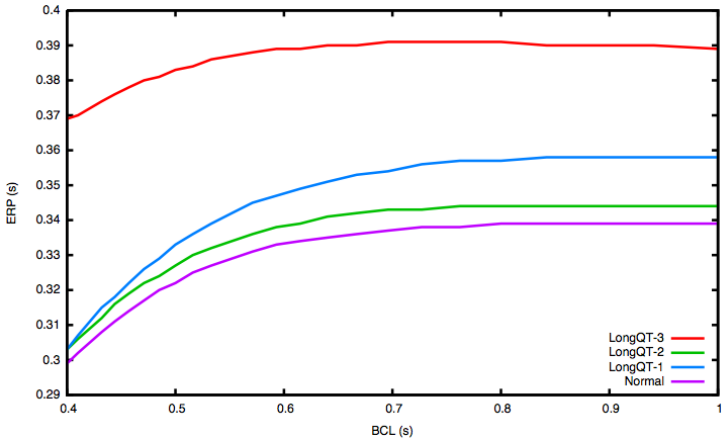

Fig. 5.5. Restitution Functions ERP represented against BCL

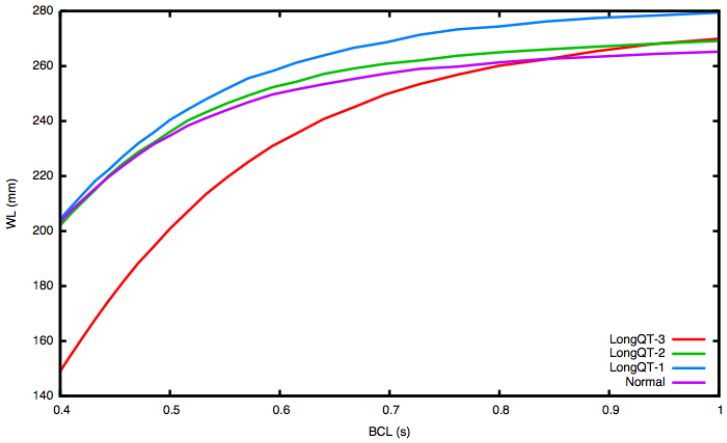

Fig. 5.6. Restitution Functions WL represented against BCL

As expected, all the action potentials for Long-QT subtypes present a prolongation (fig 5.3). This prolongation is more significant for the LQT1 case and least significant when it comes to LQT2. The CV, ERP and WL are shown in figure 5.6. The curves for the physiological case and the first two subtypes are similar, only LQT3 follows a different pattern.

5.3 Adjustment of the T-wave

To allow a visual evaluation of the T-wave for each of the heterogeneous configurations, cropped T-waves corresponding to the Einthoven II lead are shown compared to measurements in figure 5.7. All the signals were normalized to their respective R-peak amplitude in the Einthoven II lead to eliminate influences of the measurement system, which is re-

upna Universidad Pública de Navarra Nafarroako Unibertsitate Publikoa
Todos los derechos reservados
Eskubide guztiak erresalbatu dira

sponsible for the absolute signal amplitude. Signals are grouped in categories: transmural, apico-basal, diagonal, combined and g_{Kr}-reduced.

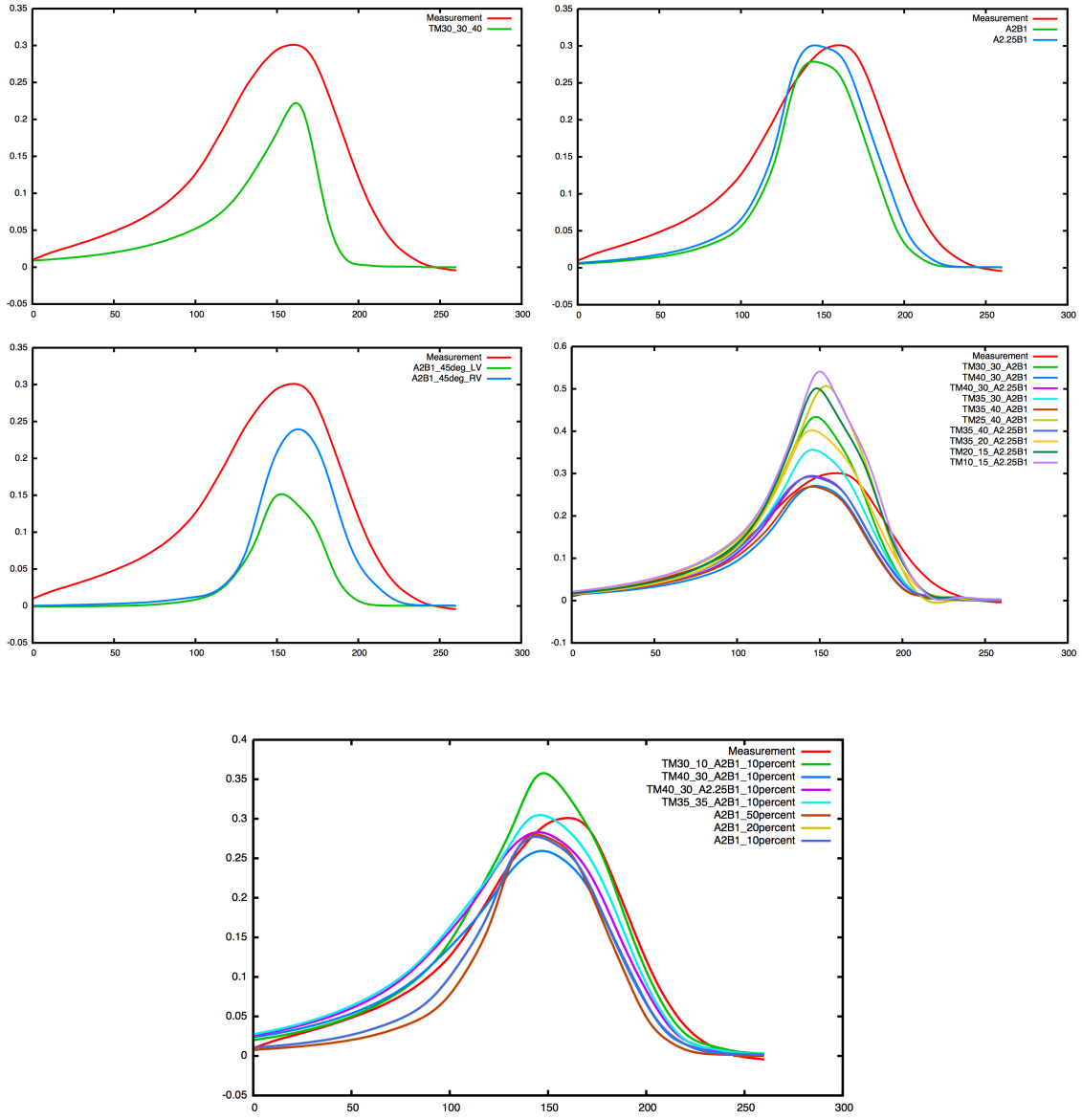

Fig. 5.7. Cropped T-waves of the Einthoven II leads for all the heterogeneous setups. Waves for transmural setups can be seen at the top left corner, for apico basals at the top right, diagonals at the mid left, combined at the mid right and g_{Kr}-reduced at the bottom

A more quantitative analysis is presented in table 5.3 where medians of the correlation coefficients and RMSEs over all electrodes between the measured and the simulated ECGs from the different heterogeneous configurations are shown in order to compare them with the measured T-Wave. These parameters were calculated in a window with only a cropped

upna Universidad Pública de Navarra Nafarroako Unibertsitate Publikoa
Todos los derechos reservados
Eskubide guztiak erresalbatu dira

T-Wave and parts of the ST segment since the QT times in each of the simulations were different. The window for the measured wave was chosen by finding the position of the maximum in an arbitrary lead with a positive T-Wave. Once that point was obtained, the starting point for the window was set to 160ms before, and the ending point to 100ms after which resulted on a 261ms-long window. For the simulated waves, on the contrary, it was necessary to find the best window position. With that purpose, the initial window was determined in the same way as for the measured wave and used as an initial guess. After that, the absolute value of the correlation coefficient between the simulated wave and the measured was calculated for each of the electrodes so that the median of those absolute coefficients could be found. Good alignment between measurements and simulations in all electrodes was represented by large values of those medians. In order to find the best plausible alignment, the window was symmetrically shifted in a 40ms interval around the T-Wave maximum. The optimum window position was chosen according to the largest value among the median of the absolute correlation coefficients for each window position.

Table 5.3. Medians of the correlation coefficients and RMSEs over all electrodes between the measured and the simulated ECGs from the different heterogeneous configurations.

Setup	Median Correlation Coefficient	Median RMSE
TM30_10_A2B1_10percent	0.93525	0.081873
A2B1_10percent	0.92226	0.073216
A2B1_20percent	0.92226	0.073216
A2B1_50percent	0.9129	0.075112
TM20_15_A2.25B1	0.90819	0.111
TM10_15_A2.25B1	0.90552	0.1176
A2B1	0.89901	0.076336
TM30_A2B1	0.89658	0.082341
TM35_30_A2B1	**0.896**	**0.079551**
TM35_20_A2.25B1	0.89581	0.087372
TM40_30_A2.25B10percent	0.87987	0.078626
TM25_40_A2B1	0.87958	0.087656
A2.25B1	0.87822	0.0813
TM35_35_A2B1_10percent	0.86901	0.072691
A2B1_45deg_LV	0.86573	0.085492
A2B1_45deg_RV	0.83026	0.072916
TM40_30_A2.25B1	0.82906	0.078969
TM30_30_40	0.82506	0.071342
TM40_A2B1	0.82236	0.070918
TM40_30_A2B1_10percent	0.81422	0.069322
TM35_40_A2B1	0.80652	0.073703
TM35_40_A2.25B1	0.79998	0.08124

upna Universidad Pública de Navarra Nafarroako Unibertsitate Publikoa
Todos los derechos reservados
Eskubide guztiak erresalbatu dira

Table 5.3 shows the median of the correlation coefficients (without absolutes in this case) and the median of the root mean square error (RMSE) in that window between each setup and the measurement. Setups are arranged by CC from bigger to smaller. The correlation coefficient just considers alignment, hence the need to calculate the RMSE to take amplitude into account. Similarly to the correlation coefficients, it was calculated over all the electrodes and the median was extracted from those values.

The best resemblance between the simulated and the measured signals is represented by a large CC and a small RMSE. Results concerning CC were on the whole very satisfactory, reaching a correlation of the 92% in the best case and 79% in the worst. As observed, setups with g_{Kr} reduction often show a higher correlation coefficient, presenting the four setups with highest values this kind of heterogeneity. However, those setups were not valid for our work, since the reduction in the conductivity causes itself a prolongation of the QT time and that would interfere with the research. Nevertheless, they provided a better understanding of the morphology of the T-wave. The setups TM20_15_A2.25B1 and TM10_15_A2.25B1 also presented fairly high CCs but the RMSE was big enough to discard them as well. As we wanted to include combined heterogeneities, A2B1 was also eliminated and between TM30_A2B1 and TM35_30_A2B1 having the last one a smaller RMSE for a similar CC, finally TM35_30_A2B1 was the chosen.

5.4 BSPM Analysis

After developing cell models for the Long-QT subtypes and adjusting the T-wave by choosing a setup to model the physiological heterogeneity, Body Surface Potential Maps (BSPM) were simulated all over the thorax for the physiological case and the three subtypes. Nodes were chosen so that the minimum distance among them was 1.7cm leading to 1050 nodes, thus, 1050 signals for each of the cases.

Einthoven leads for all the cases are compared in figure 5.8-5.10 to get a visual concept of the simulated ECGs. All the subtypes show a prolongation in the QT time, although less significant than expected, specially for LQT-2 and LQT-3. For comparative reasons, the average QT time was calculated over the 1050 nodes. With that purpose it was necessary to determine the T_{end} time, which corresponds to the end of the T-wave. There are different methods to determine this point and we used a variant of the so called tangent method. A tangent line to the steepest point of the descending limb of the T wave was constructed and the end of the T wave was defined as the point where this line intersected zero. This was done over all the signals and it is important to note that not all of them had positive T-waves, but also negative and biphasic. In any case, the method was the same, only negative T-waves and biphasic T-waves with a notch after an initial peak

upna Universidad Pública de Navarra Nafarroako Unibertsitate Publikoa
Todos los derechos reservados
Eskubide guztiak erresalbatu dira

were turned upside down before the method was applied. The mean of the QT time was calculated over all the signal set.

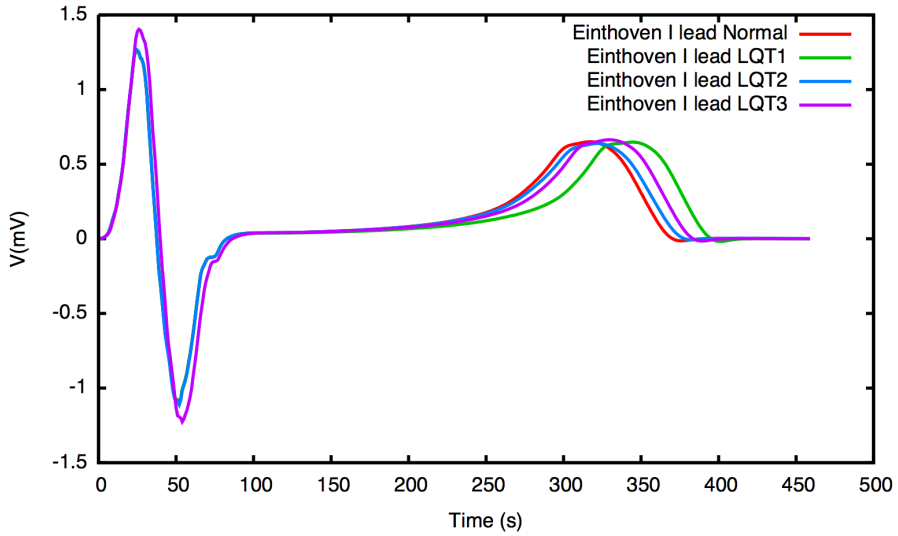

Fig. 5.8. Einthoven lead I for the simulated BSPM including the normal case and the three Long-QT subtypes.

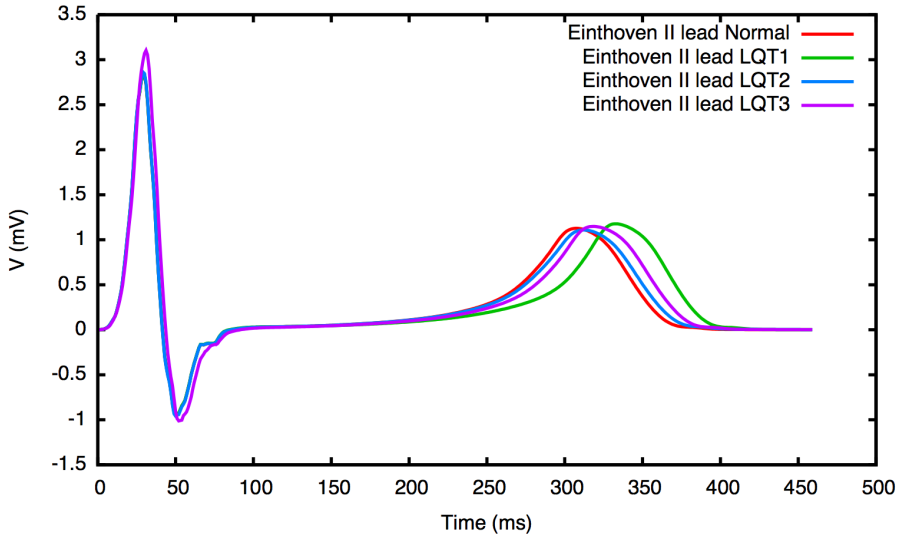

Fig. 5.9. Einthoven lead II for the simulated BSPM including the normal case and the three Long-QT subtypes.

upna Universidad Pública de Navarra Nafarroako Unibertsitate Publikoa
Todos los derechos reservados
Eskubide guztiak erresalbatu dira

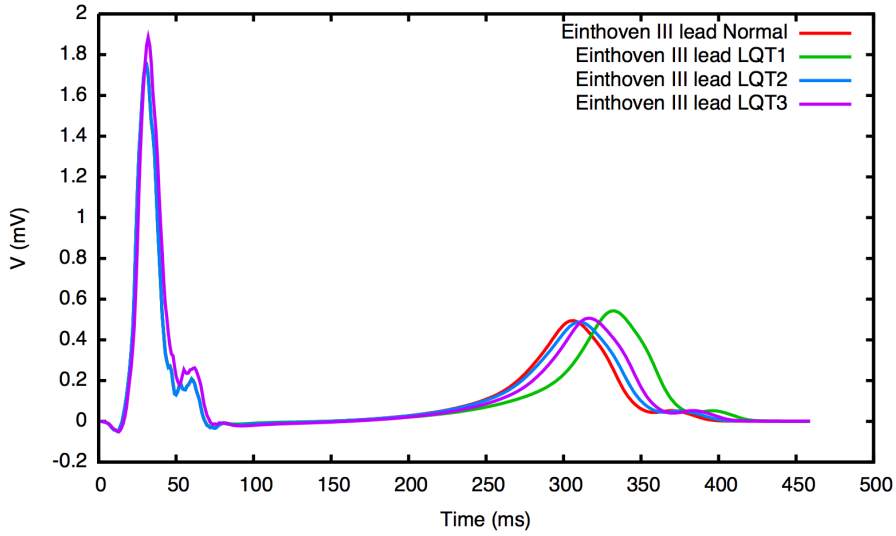

Fig. 5.10. Einthoven lead III for the simulated BSPM including the normal case and the three Long-QT subtypes.

Table 5.4 shows the average QT times for all the cases. As expected, this time is longer for the subtypes, being the longest for LQT-1 and the shortest for LQT-2. However, they still don't fit reality in an accurate way, since prolonged QT times appear to be shorter than realistic QT times for the Long-QT syndrome [51].

Table 5.4. Average QT times for the normal case and the three subtypes

	Normal	**LongQT-1**	**LongQT-2**	**LongQT-3**
Avg QT time (ms)	380.1560	404.9741	386.1057	393.5384

5.4.1 Differences Between Subtypes

The first approach to determine if there were differences between each subtype was the subtraction of signals. Being just the T-wave the point of our interest, the QRS complex was eliminated from the signals and our analysis was focused on a cropped T-wave. Subtypes were arranged in pairs (LQT-1 to LQT-2, LQT-1 to LQT-3 and LQT-2 to LQT-3) and the subtype with the longest QT time was shifted the averaged shifted time, which was calculated over the 1050 signals as well. Once we got the T-waves lying on top of each other, a regular subtraction was performed. As our interest was not quantitative regarding the values of the differences, we focused on identifying the nodes in which the differences were maximal and enumerated ten of them (table 5.5 shows them for all the cases and arranged by absolute differences in a descendant way).

upna Universidad Pública de Navarra Nafarroako Unibertsitate Publikoa
Todos los derechos reservados
Eskubide guztiak erresalbatu dira

Table 5.5. Numbers identifying the nodes in which the differences between subtypes are more significant

LQT1 to LQT2	LQT1 to LQT3	LQT2 to LQT3
176967	1232	176967
10766	278176	23457
75970	59187	75970
83	351375	83
11049	23457	64700
323596	42096	20668
38540	34981	1232
73008	64700	18393
14255	9390	323596
267405	7406	11049

Note how some nodes appear in both LQT-1 to LQT-2 and LQT-2 to LQT-3 in the same positions, *i.e* 176967 shares first position in both cases, 75970 is third and 83 fourth. That gives us an idea about the regions where the differences are significant being similar for both cases. A more visual analysis of the differences can be seen in appendix B, where evolutions of the ECGs can be found. First, voltages during the T-wave are displayed for each of the subtypes (LQT-1, LQT-2 and LQT-3) and, after, the voltages resulting from the subtraction (explained above) are displayed for each of the compared cases.

5.4.1.1 Descriptors for the Morphology of the T-wave

The subtraction of T-waves gives an idea about differences in amplitude, but differences in the morphology of the wave are also interesting to compare. Due to difficulties to choose correct descriptors for biphasic waves, only monophasic waves were analyzed with this procedure. Negative waves were twisted to make the analysis easier. With that in mind, we chose 3 descriptors: kurtosis, skewness and flatness, being the flatness the difference between the T_{end} time and the time correspondent to the maximum peak of the wave.

To perform a correct comparison of the mentioned descriptors, T-waves needed to be cropped in such a way that the window was equally sized for all of them and the peak of the wave was located exactly in the middle. The window size was determined by the wave with maximum T_{peak}-T_{end} distance. Once that wave was found, the end point of the window was chosen to be 102% of its T_{end} and the window length was set to double the distance from T_{peak} to the end point. All signals were cropped according to that size, the kurtosis, skewness and flatness were calculated and differences between these parameter values were computed for all the comparison cases. As for the differences, our interest was not quantitative regarding the values of the descriptors so we focused on identifying the nodes in which the differences between parameters were maximal and enumerated

upna Universidad Pública de Navarra Nafarroako Unibertsitate Publikoa
Todos los derechos reservados
Eskubide guztiak erresalbatu dira

four nodes for each descriptor. Tables 5.6, 5.7 and 5.8 show the numbers of those nodes arranged by values of the differences in a descendant way.

Table 5.6. Kurtosis. Numbers of the nodes in which the differences between subtypes are more significant

	LQT1 to LQT3	**LQT2 to LQT3**
9702	31494	31494
15623	9702	282462
31494	282462	25529
11987	11987	145224

Table 5.7. Skewness. Numbers of the nodes in which the differences between subtypes are more significant

	LQT1 to LQT3	**LQT2 to LQT3**
15623	31494	31494
27921	15623	282462
31494	27921	19026
176967	282462	265807

Table 5.8. Flatness. Numbers of the nodes in which the differences between subtypes are more significant

	LQT1 to LQT3	**LQT2 to LQT3**
9702	267488	267488
83	83	265807
27921	9702	19026
176967	176967	305917

upna Universidad Pública de Navarra Nafarroako Unibertsitate Publikoa
Todos los derechos reservados
Eskubide guztiak erresalbatu dira

6

Summary

Long-QT syndrome affects up to 1 out of 2500 people and it's a common cause of sudden cardiac death among children and young population. Diagnosis and subtyping developed methods so far are not as accurate as desired, though. Being genetic testing the main subtyping procedure and the fact that many Long-QT-causing mutations still remain undiscovered are possible reasons to explain the lack of accuracy. Hence the need to think of alternative ways to face this disorder.

Researchers in the Institute of Biomedical Engineering at the Karlsruhe Institute of Technology [52] brought up the possibility to distinguish between Long-QT subtypes by investigating extracellular potential distributions in BSPM. In this work, this possibility was examined and thoroughly studied by developing Long-QT related cell models and simulating BSPM.

For that reason, channel kinetics related to pathological mutations were adjusted and integrated into the Ten Tusscher model for ventricular myocytes. LQT-1 and LQT-2 were adjusted by extracting current-voltage graphs from literature, and a parameter optimization regarding steady state time constants and activation and inactivation curves was performed. Simulations resulted in smaller values of the conductivity and changes in gating constants, slightly more significant in the LQT-1 case. The LQT-2 data turned out to be a bit more difficult to fit. The LQT-3 was integrated by using the Markov chain that Clancy and Rudy presented in [39]. Simulated APD showed, indeed, that the Long-QT cell models provoked a prolongation of the action potential duration. However the LQT-2 case didn't fulfill our expectations.

In parallel to that task, it was necessary to adjust the T-wave to measured BSPM by distributing I_{Ks} heterogeneously throughout the ventricles. Taking [45] as a basis, 22 different heterogeneous g_{Ks} distributions were created, leading to different types of DOR: Transmural, Apico-Basal, Diagonal and g_{Kr} reduced. On the whole, high correlation was

upna Universidad Pública de Navarra Nafarroako Unibertsitate Publikoa
Todos los derechos reservados
Eskubide guztiak erresalbatu dira

achieved when compared to measurements, being 92 % the highest correlation coefficient and 72 % the lowest. The RMSE values were acceptable, although still a bit higher than desired. The g_{Kr} reduced group showed higher correlation coefficients when compared to the actual T-wave, which enables a new approach to the understanding of the T-wave, since it shows that toggling not only g_{Ks} but also g_{Kr} has effects on it. However, as the g_{Kr} reduction has an effect on the QT time, we discarded those configurations when choosing the best one for our study. Although none of the tested configurations was able to reproduce the measured wave completely, a combined transmural and apico-basal setup with 35% of Endo, 30% of M and 35% of Epi cells was chosen due to its high correlation coefficient and acceptable RMSE.

The last step of this study involved the simulation of BSPM including the subtypes and the selected heterogeneous g_{Ks} distribution. 1050 nodes on the body surface were picked and ECGs were obtained from simulations. Being our interest to make a distinction between subtypes, we arranged the syndromes in pairs (LQT-1 to LQT-2, LQT-1 to LQT-3 and LQT-2 to LQT-3) and performed two different analysis. Regular signal subtraction showed that the order in the magnitude of the differences was around 1% of the order of magnitude of the voltage values themselves (see appendix B). Nevertheless, it was possible to visualize different patterns in each of the compared cases (see appendix C) and so specific electrodes in the a small area could be pointed as potential discrimination sources. When it comes to morphological evaluation, three descriptors were elected to perform our study: kurtosis, skewness and flatness. Appendix B shows that T-waves extracted from the same nodes present more similarities than differences. Anyhow, electrodes could also be elected after computing the differences in the mentioned descriptors.

The results obtained in this study show that further research is needed in this area, because even though differences were found between BSPM distributions for each subtype, the magnitude of these non similarities is smaller than desired and might not be enough to state that there is a possibility to distinguish subtypes via BSPM. In any case, a better understanding of the g_{Ks} distribution concerning the T-wave was provided and new paths were opened to future investigations.

upna Universidad Pública de Navarra Nafarroako Unibertsitate Publikoa
Todos los derechos reservados
Eskubide guztiak erresalbatu dira

7

Discussion and Outlook

The results in this work are not significant enough to make definitive statements regarding the possibility to distinguish between Long-QT subtypes by BSPM in certain electrodes. However, it provided a start point for future research and opened a path regarding the understanding of the T-wave.

The selected data regarding LQT-2 turned out not to be the best choice, leading to a complicated adjustment and not a very good example of APD prolongation. It would be desirable, thus, to find another source for I_{HERG} measurements and develop a cell model in which the altered constants resembled the LongQT syndrome type 2 in a better way. Better adjustments could have probably been achieved by including more parameters in the optimization process. Nonetheless, the aim of this work was to try to emulate reality in the best possible way, hence not many parameters being toggled.

Regarding the T-wave adjustment, reproducing the measured signal was a challenging task. Better approximations still remain to be achieved, although some of the tested configurations led to satisfactory results. It is difficult to predict how different types of DOR affect the shape of the T-wave, specially regarding transmural setups, where the effects of moving M-cells closer to the epicardium or the endocardium, or having a smaller amount of M-cells are still not very clear. When it comes to apico-basal setups, though, an increase in the gradient appears to cause an enlargement of the T-wave amplitude. All the setups fail at resembling the width of the measurements, but a reduction in g_{Kr} seemed to increase the width without provoking a prominent alteration in the amplitude. Therefore, it would be interesting to continue research in this direction.

The simulated BSPM for the Long-QT subtypes were concordant when compared to the simulated physiological case, presenting all of them the expected enlargement on the QT time. However, there is still work to do, since neither of the cases matches reality (QT times appear shorter that they are in measured ECGs). Definitions of normal QT varies

upna Universidad Pública de Navarra Nafarroako Unibertsitate Publikoa
Todos los derechos reservados
Eskubide guztiak erresalbatu dira

around being equal to or less than 400 [53], 410 [54], 420 [55] or 440 miliseconds [56]. An abnormal QT in males is a QT time above 450 ms, and in females, above 470 ms [51]. Consequently, taking a look at table 5.4 it can be seen how our QT times are shorter than realistic.

Furthermore, depending on the observed body surface point, the T-waves could be classified in monophasic positive, monophasic negative or biphasic. An interesting characteristic that emerged from this work is the concordance between T-waves resulting from different types in the same nodes. For instance, waves extracted from the same node would belong to the same class in most of the cases and present very little differences. In spite the fact that they were very small, it was still possible to extract specific electrodes presenting more detectable dissimilarities and to observe patterns in the distribution of the T-waves and the T-wave differences. However, better data gathering and further research would clarify the black spots in this work.

In conclusion, the hypothesis of detecting Long-QT subtypes via BSPM still remains plausible, even though further investigation is needed.

upna Universidad Pública de Navarra Nafarroako Unibertsitate Publikoa
Todos los derechos reservados
Eskubide guztiak erresalbatu dira

A

T-Wave Comparison

With the purpose of allowing a clearer view of the T-waves for the different heterogeneous distributions explained in section 4.3, the following figures are an expanded version of figure 5.7. It is important to keep in mind that this allows a mere visual evaluation and that what appears here is just the Einthoven II lead. Therefore, if some of the results here seem to mismatch the quantitative analysis in table 5.3 it is important to remember that the CC and RMSE have been calculater over all the leads.

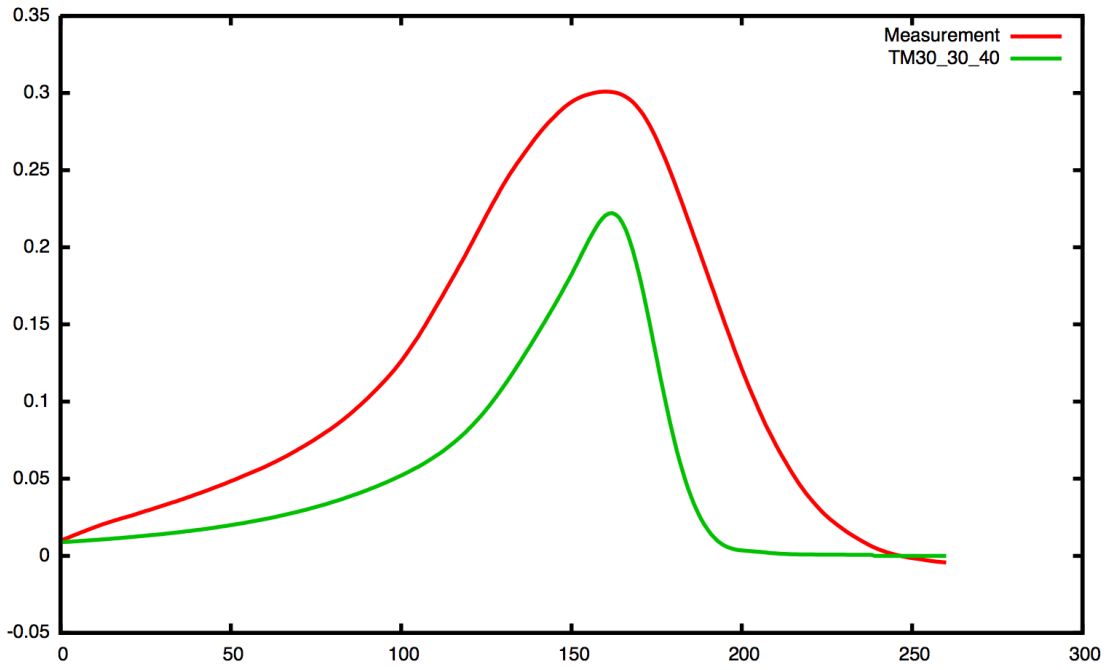

Fig. A.1. Cropped T-waves of the Einthoven II leads for setups with transmural heterogeneities.

upna Universidad Pública de Navarra Nafarroako Unibertsitate Publikoa
Todos los derechos reservados
Eskubide guztiak erresalbatu dira

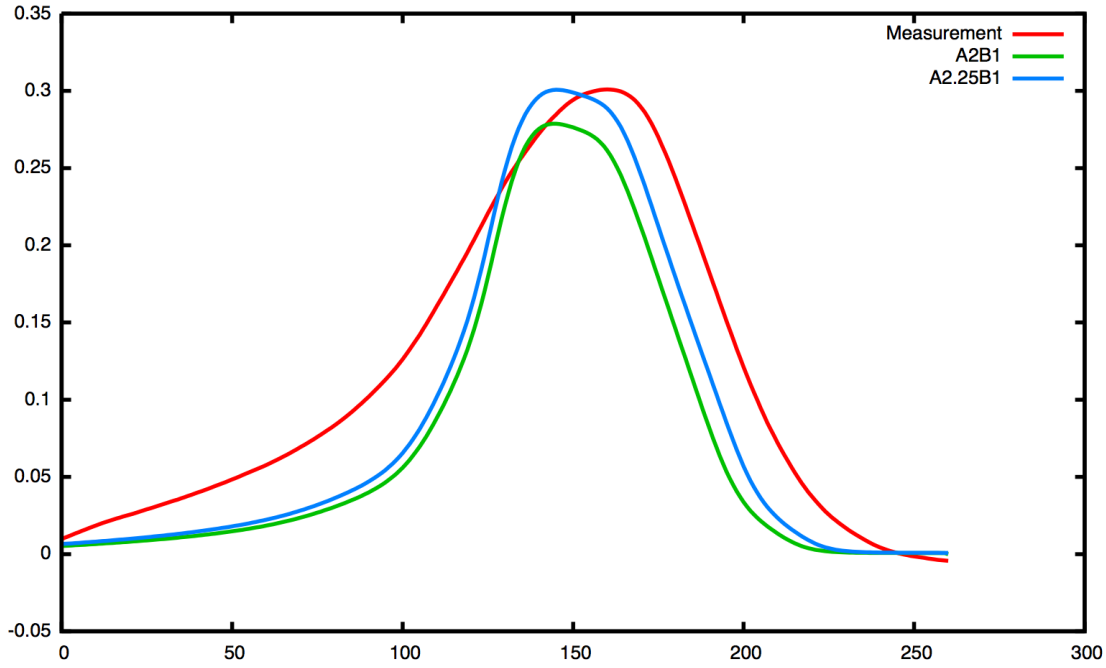

Fig. A.2. Cropped T-waves of the Einthoven II leads for setups with apico-basal heterogeneities.

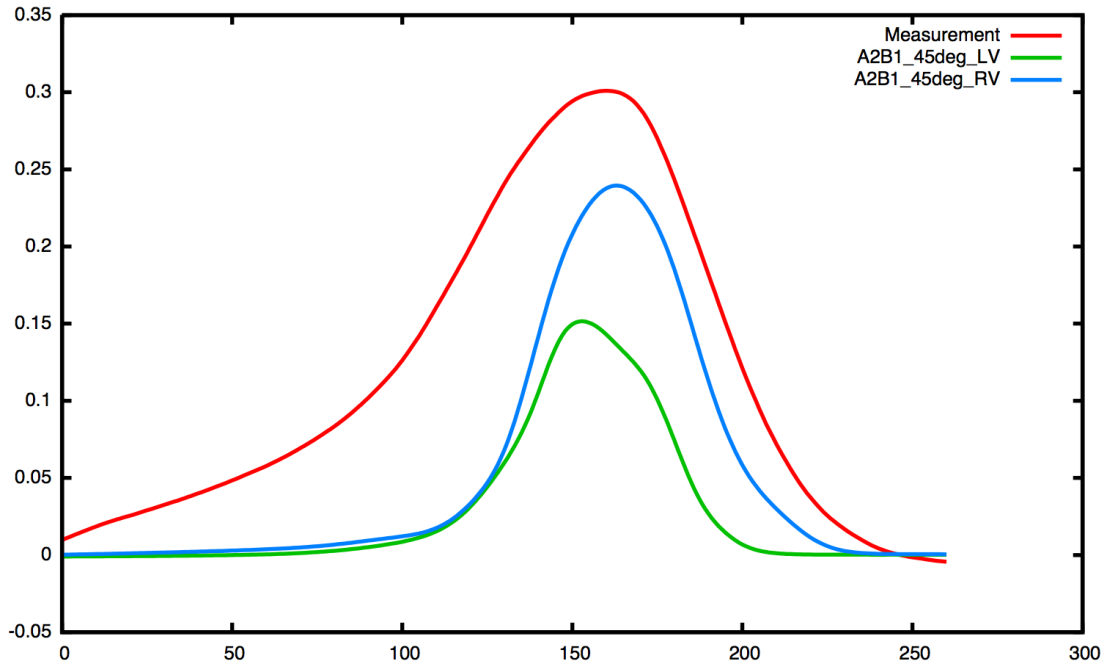

Fig. A.3. Cropped T-waves of the Einthoven II leads for setups with diagonal heterogeneities.

upna Universidad Pública de Navarra Nafarroako Unibertsitate Publikoa
Todos los derechos reservados
Eskubide guztiak erresalbatu dira

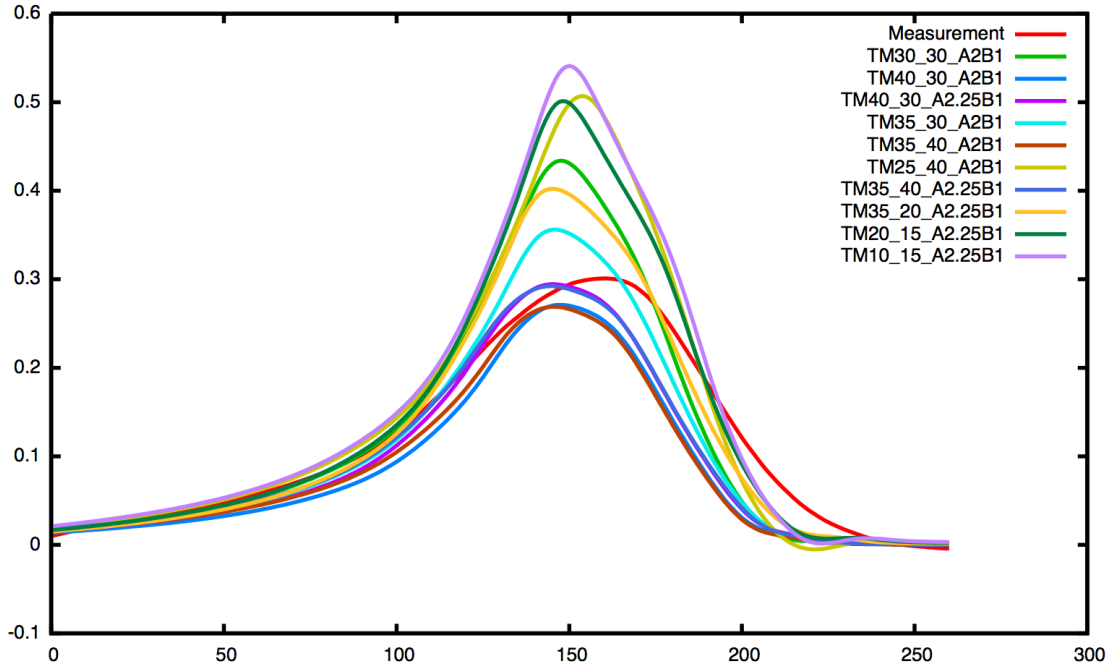

Fig. A.4. Cropped T-waves of the Einthoven II leads for setups that combine both apico-basal and transmural heterogeneities.

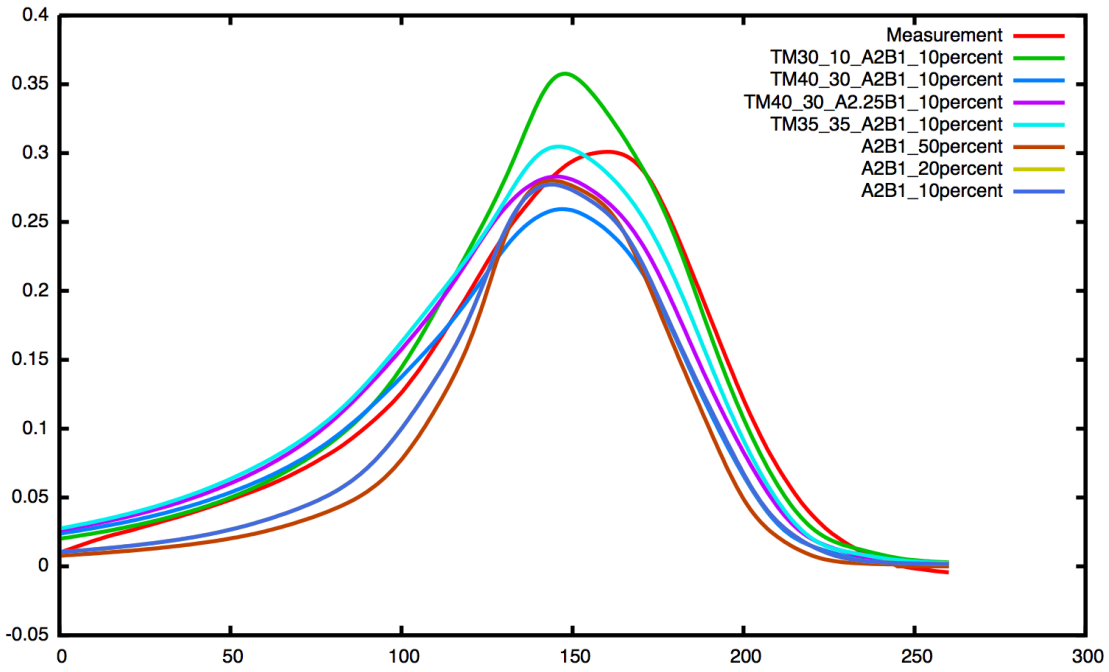

Fig. A.5. Cropped T-waves of the Einthoven II leads for setups with reduced g_{Kr}.

upna Universidad Pública de Navarra Nafarroako Unibertsitate Publikoa
Todos los derechos reservados
Eskubide guztiak erresalbatu dira

upna Universidad Pública de Navarra Nafarroako Unibertsitate Publikoa
Todos los derechos reservados
Eskubide guztiak erresalbatu dira

B

T-Wave Analysis 1

In order to have a visual perception of the differences between subtypes regarding the T-waves, subtypes were arranged in pairs and the differences were computed. Once that was done, the 10 nodes in which the differences were maximum were selected. The following figures show the T-waves in those nodes after times were shifted and the T-waves laid on top of each other.

upna Universidad Pública de Navarra Nafarroako Unibertsitate Publikoa
Todos los derechos reservados
Eskubide guztiak erresalbatu dira

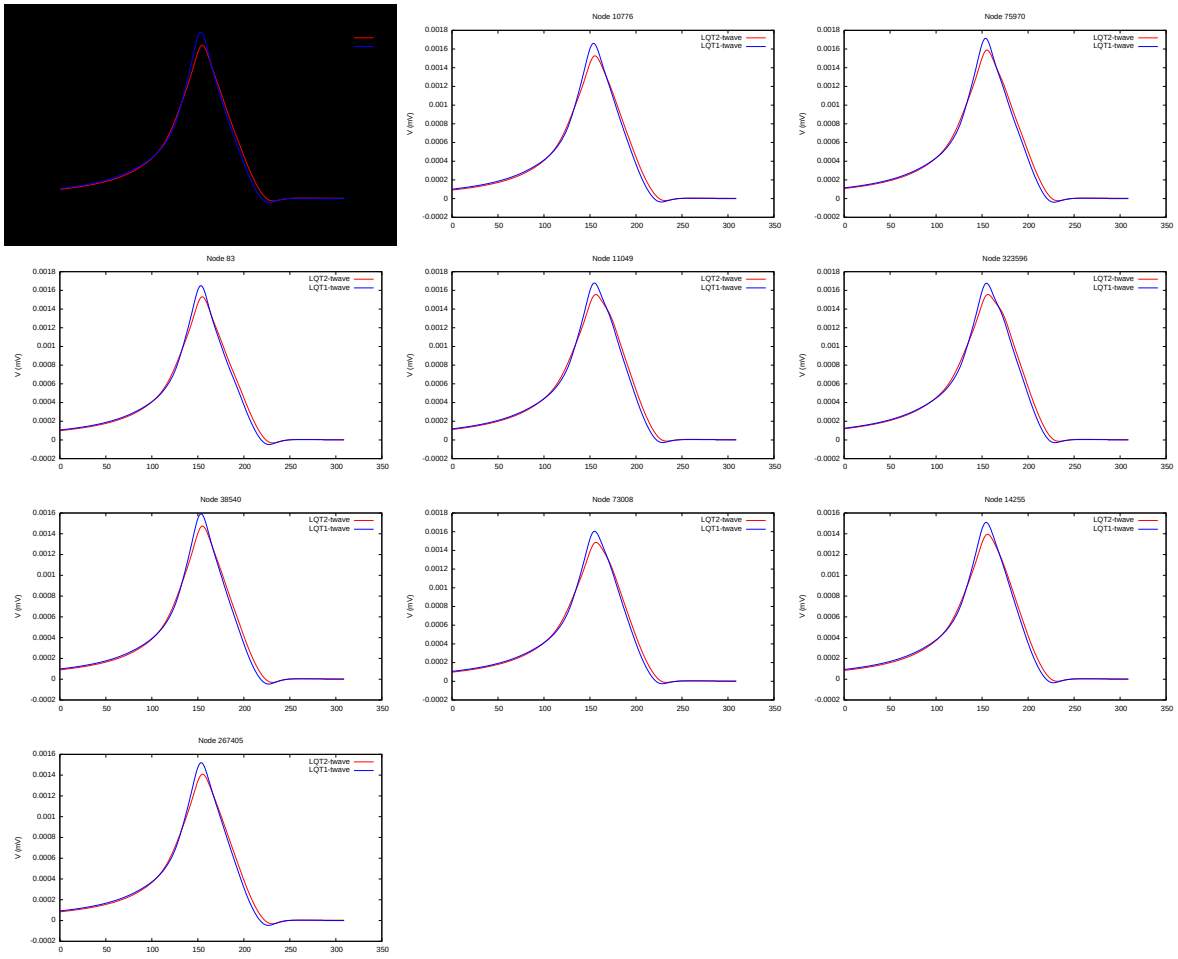

Fig. B.1. Each of the plot shows LQT-1 and LQT-2 waves after LQT-2 waves were shifted so that they laid on top of each other. The node numbers correspond to the 10 nodes in which differences between those specific subtypes were more significant.

upna Universidad Pública de Navarra Nafarroako Unibertsitate Publikoa
Todos los derechos reservados
Eskubide guztiak erresalbatu dira

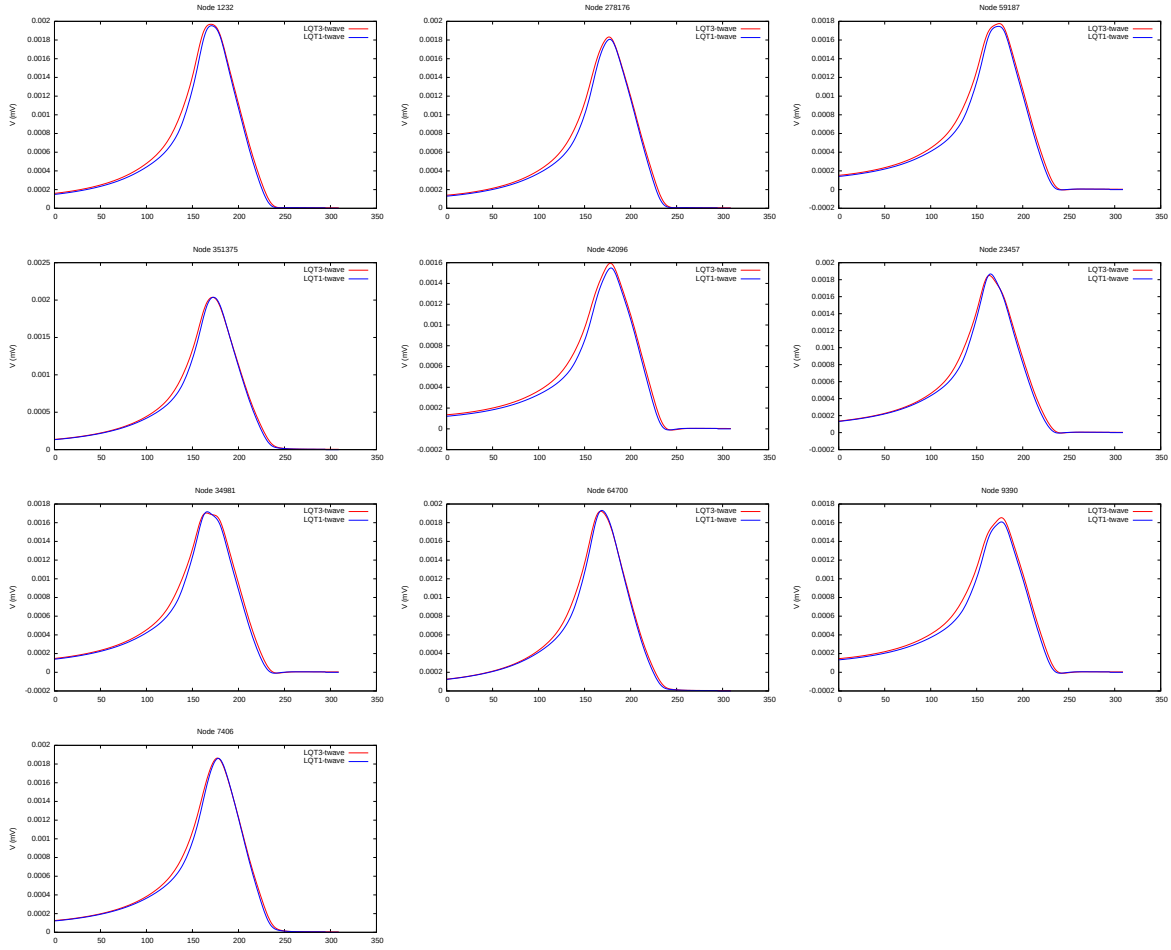

Fig. B.2. Each of the plot shows LQT-1 and LQT-3 waves after LQT-3 waves were shifted so that they laid on top of each other. The node numbers correspond to the 10 nodes in which differences between those specific subtypes were more significant.

upna Universidad Pública de Navarra Nafarroako Unibertsitate Publikoa
Todos los derechos reservados
Eskubide guztiak erresalbatu dira

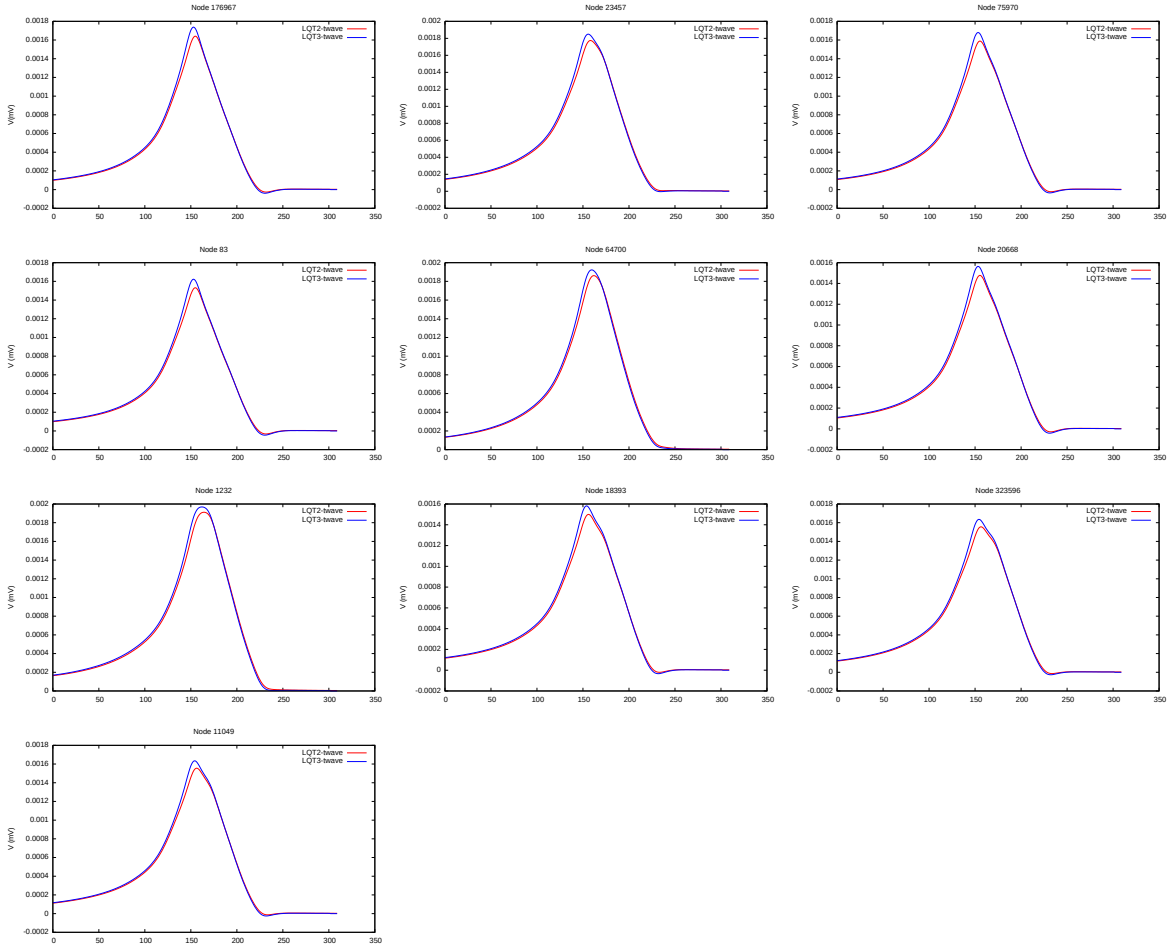

Fig. B.3. Each of the plot shows LQT-3 and LQT-2 waves after LQT-2 waves were shifted so that they laid on top of each other. The node numbers correspond to the 10 nodes in which differences between those specific subtypes were more significant.

upna Universidad Pública de Navarra Nafarroako Unibertsitate Publikoa
Todos los derechos reservados
Eskubide guztiak erresalbatu dira

C

T-wave Analysis 2

The extracellular potentials during the T-wave were interpolated onto the thorax surface for each of the subtypes so that a visual evaluation could be achieved. Figures C.1, C.2 and C.3 show the 3D evolution of the voltages along the thorax, whereas figures C.4, C.5 and C.6 show a 3D evolution but of the differences between subtypes calculated as described in section 5.4.1. For those figures, electrodes in which the differences were significative are also displayed to have an idea of the region where the dissimilarities are detectable.

Temporal sequences for the T-wave only (from millisecond 125 to millisecond 235) are shown in all figures (from figure C.1 to figure C.6). The timestamps are the same in all of them and there is a 10ms difference between each adjacent image. Slightly different patterns can be distinguished for the three comparisons.

upna Universidad Pública de Navarra Nafarroako Unibertsitate Publikoa
Todos los derechos reservados
Eskubide guztiak erresalbatu dira

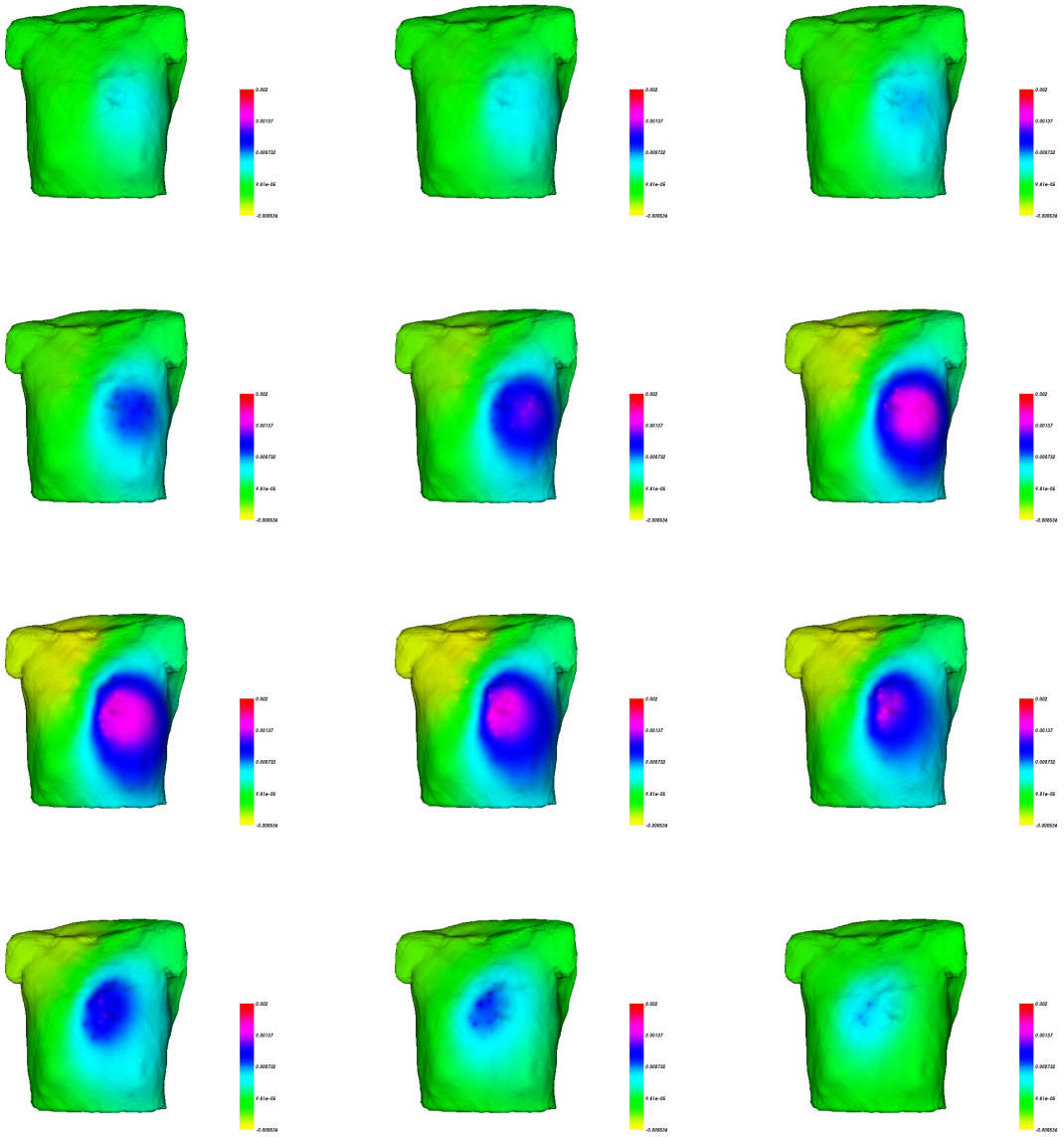

Fig. C.1. LQT-1. 3D evolution representation of the simulated extracellular potentials during the T-wave

upna Universidad Pública de Navarra Nafarroako Unibertsitate Publikoa
Todos los derechos reservados
Eskubide guztiak erresalbatu dira

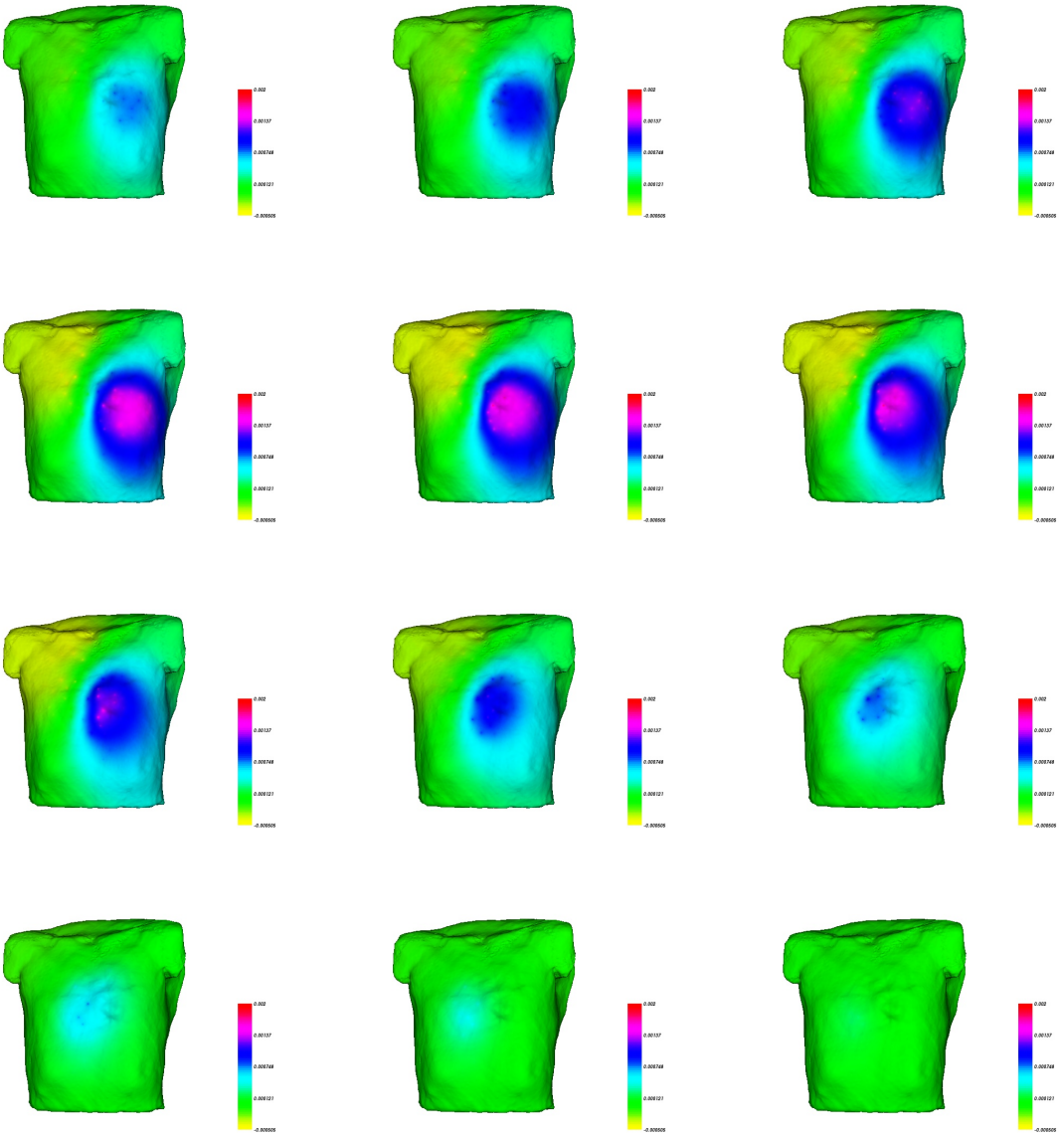

Fig. C.2. LQT-2. 3D evolution representation of the simulated extracellular potentials during the T-wave

upna Universidad Pública de Navarra Nafarroako Unibertsitate Publikoa
Todos los derechos reservados
Eskubide guztiak erresalbatu dira

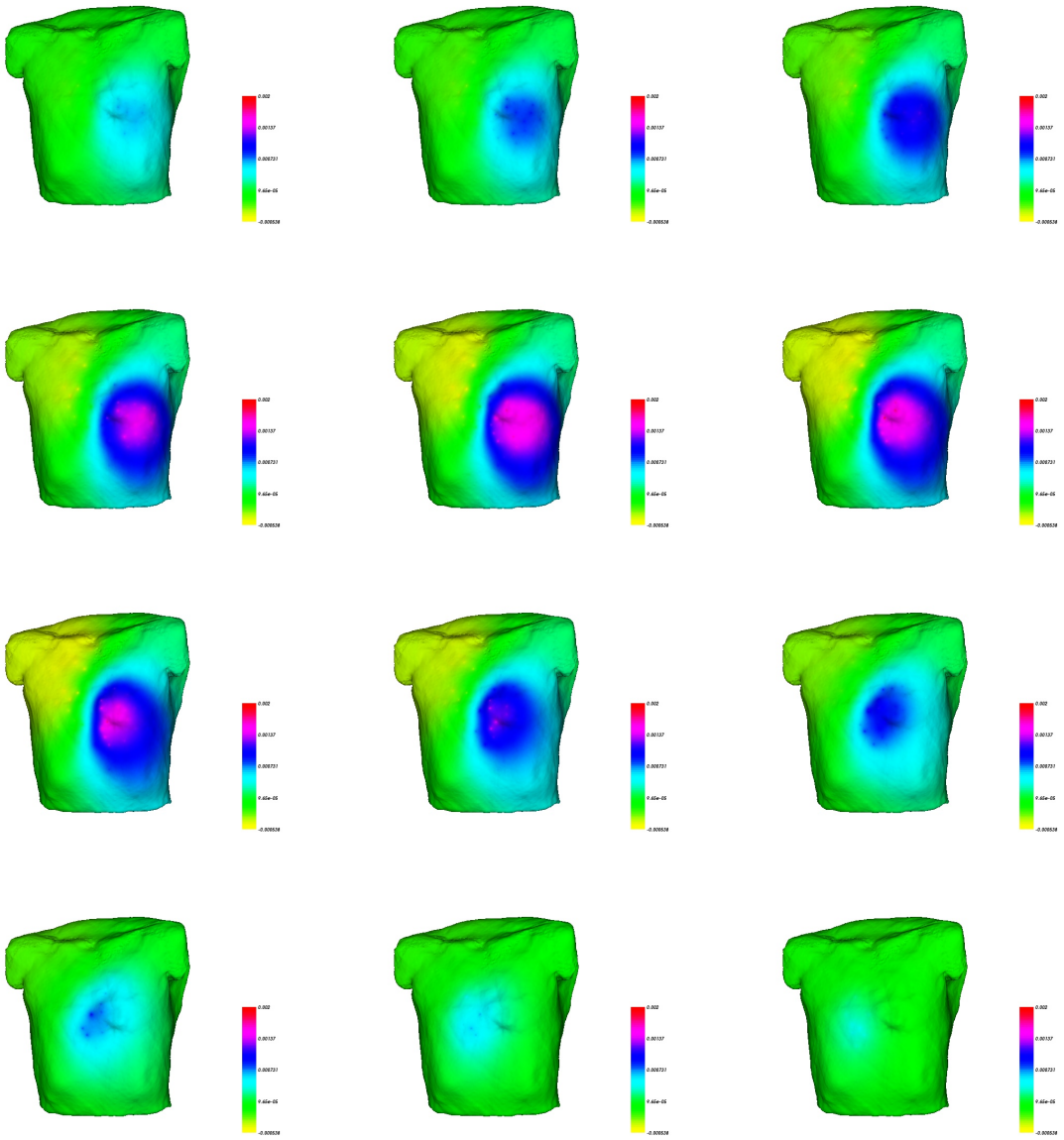

Fig. C.3. LQT-3. 3D evolution representation of the simulated extracellular potentials during the T-wave

upna Universidad Pública de Navarra Nafarroako Unibertsitate Publikoa
Todos los derechos reservados
Eskubide guztiak erresalbatu dira

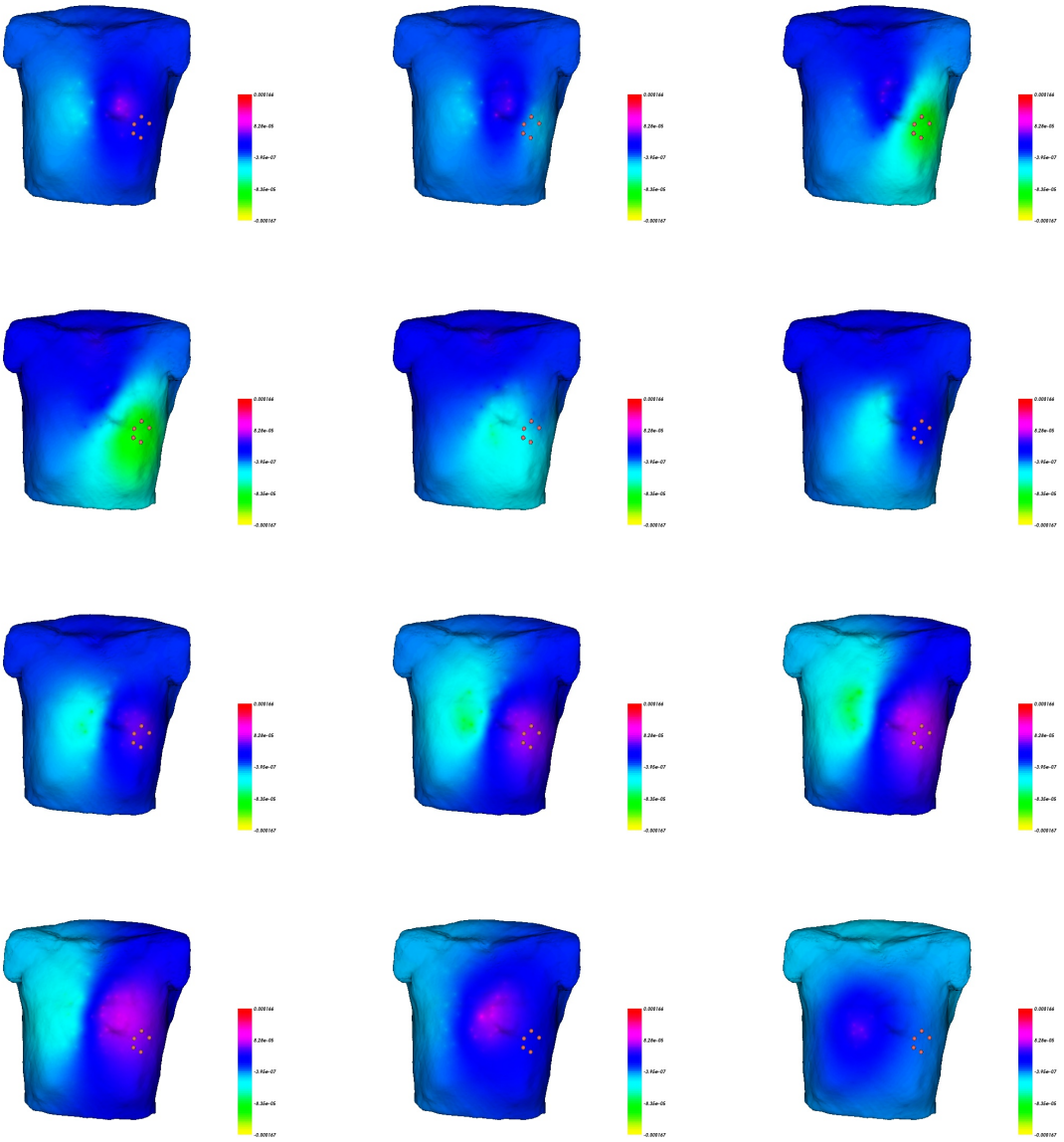

Fig. C.4. Substraction of LQT-2 to LQT-1. 3D evolution representation of the simulated extracellular potentials during the T-wave

upna Universidad Pública de Navarra Nafarroako Unibertsitate Publikoa
Todos los derechos reservados
Eskubide guztiak erresalbatu dira

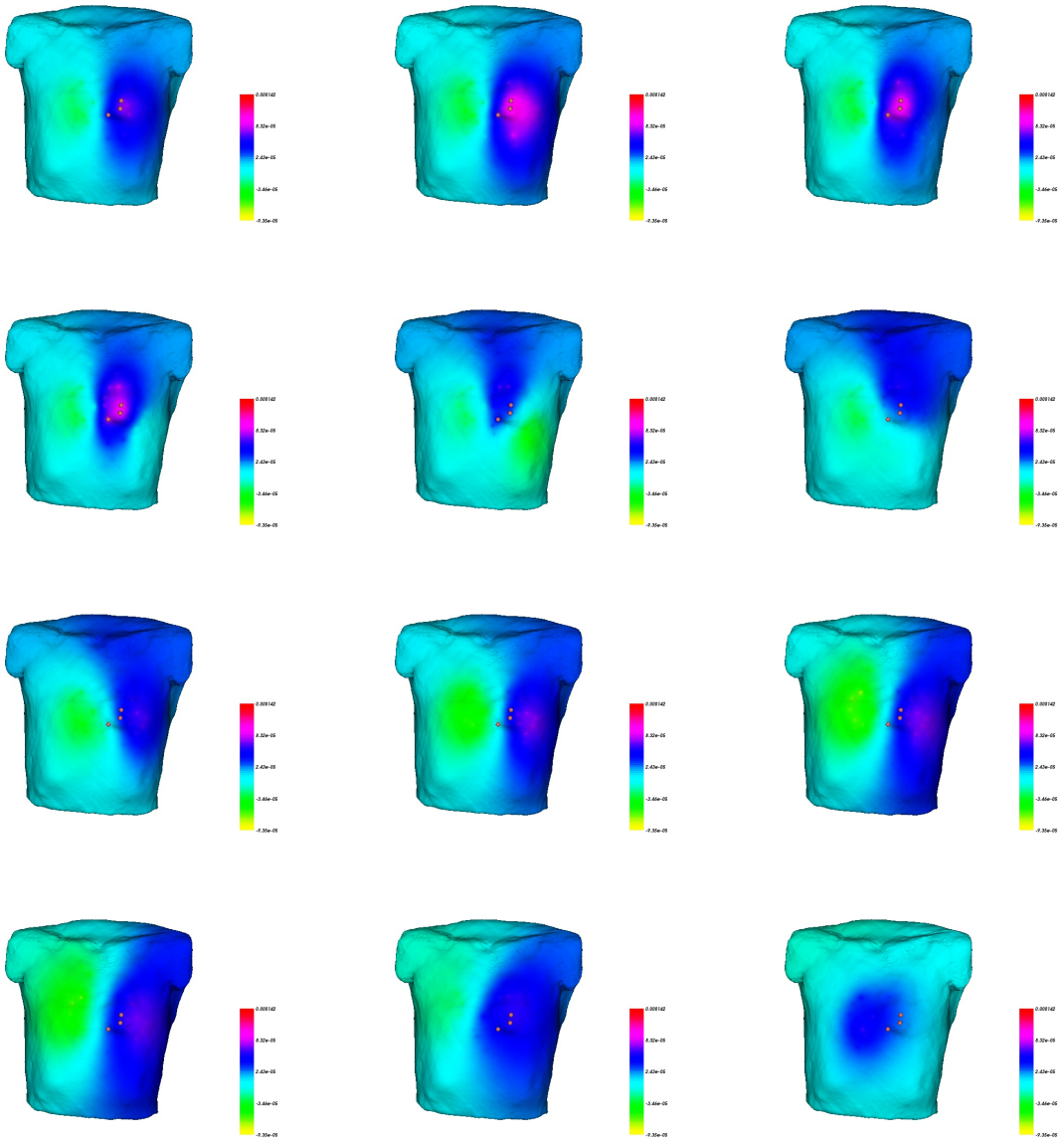

Fig. C.5. Substraction of LQT-3 to LQT-1. 3D evolution representation of the simulated extracellular potentials during the T-wave

upna Universidad Pública de Navarra Nafarroako Unibertsitate Publikoa
Todos los derechos reservados
Eskubide guztiak erresalbatu dira

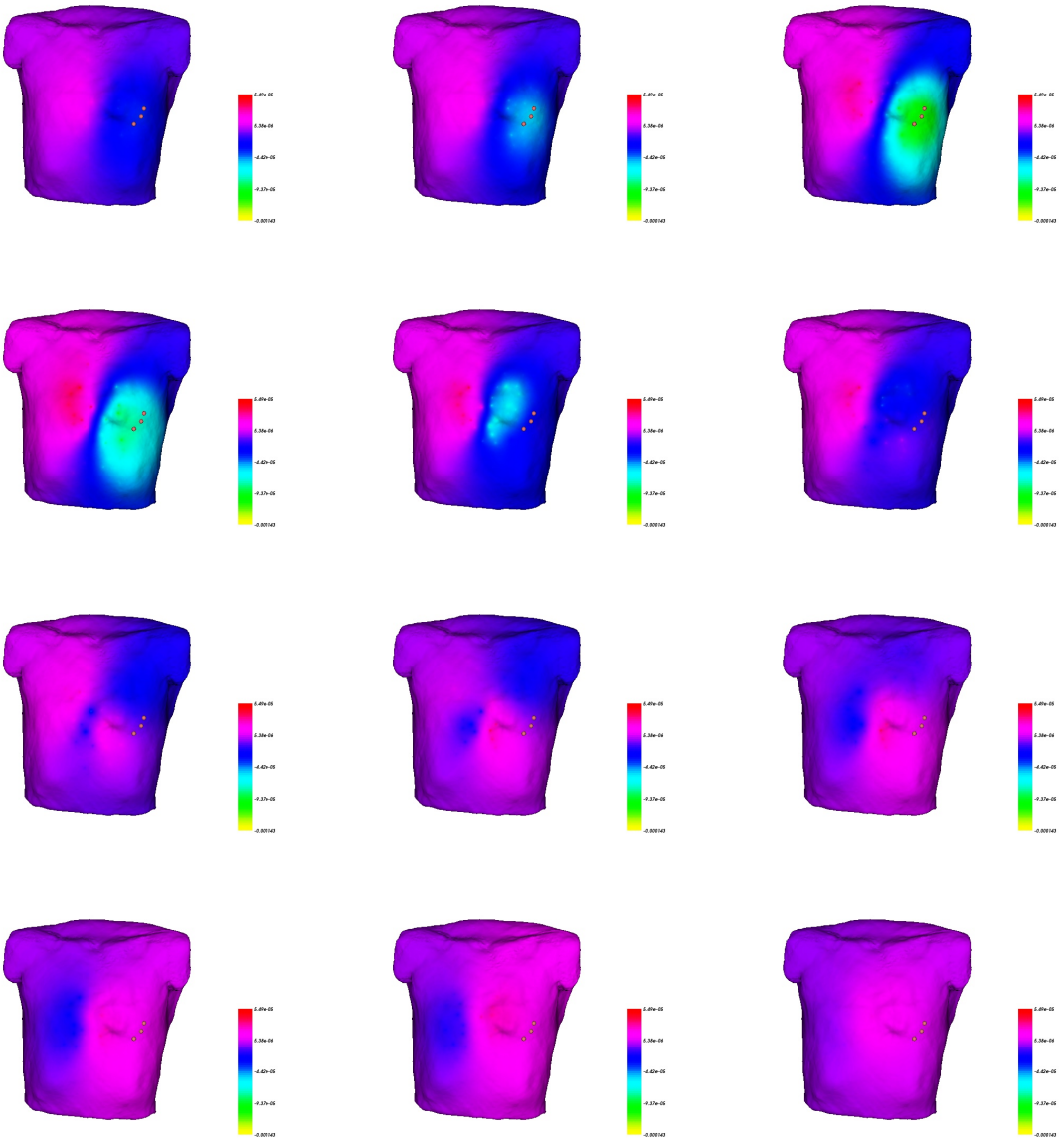

Fig. C.6. Substraction of LQT-3 to LQT-2. 3D evolution representation of the simulated extracellular potentials during the T-wave

upna Universidad Pública de Navarra Nafarroako Unibertsitate Publikoa
Todos los derechos reservados
Eskubide guztiak erresalbatu dira

upna Universidad Pública de Navarra Nafarroako Unibertsitate Publikoa
Todos los derechos reservados
Eskubide guztiak erresalbatu dira

Acknowledgments

This diploma thesis was conducted at the Institute of Biomedical Engineering at Karlsruhe Institute of Technology (KIT).

I would like to thank Prof. Dr. Olaf Dössel for giving me the opportunity to take part in this project under his guidance. My special thanks to Gunnar Seemann and David Keller not only for their exceptional supervision and the amount of time they invested in my project but for being patient and supportive as well. They were always willing to listen, help and comfort and I have learned a lot thanks to their knowledge.

Being the IBT my second home (even my first home at the end) how could I not mention my fellow students in the Diplomandenraum. Thanks for those kaffeepauses, for sharing laughters, insults and cigarettes with me and bearing me even though I sometimes get on your nerves.

This work has been a challenge for me, not only because of the project itself but also due to the fact that I was away from home. For that reason I would have never been able to accomplish this without the help of what here in Karlsruhe has been my alternative family. Thanks from deep in my heart to Zoo on Fire and AbbaMole (too many names to write all!!) and a special mention to Tina Bautović for being friend, sister and mother when I needed. Also to Jota, who had to suffer the pressure of this thesis as if it was his own work.

For their support in the distance and their great friendship throughout these years, thanks a lot to my friends and classmates back home. To Idoia, for 23 years of friendship in which she never failed to be there for me. Amaia, for the constant support and care. Aitor (er Dele) for laughing at all my nervous attacks. Kuadrilla, Corderas (plus peñita txoko) and ElGroupo (again too many names), also in mind.

upna Universidad Pública de Navarra Nafarroako Unibertsitate Publikoa
Todos los derechos reservados
Eskubide guztiak erresalbatu dira

Above all, I would like to thank my family for supporting and bearing me all this time. They always believed in me and gave up many things so that I could have the opportunities they didn't have. Thanks mum, dad, Laura, Natalia, Ainara, Diego, Rafa, Lucía, Martín and Marina for being who they are.

Eskerrik asko guztioi!

upna Universidad Pública de Navarra Nafarroako Unibertsitate Publikoa
Todos los derechos reservados
Eskubide guztiak erresalbatu dira

References

1. "http://www.childrenshospital.org/az/site507/mainpages507p0.html."
2. B. Alberts, A. Johnson, J. Lewis, M. Raff, K. Roberts, and P. Walter, *Molecular Biology of the Cell*. New York: Garland Science, 4th ed., 2002.
3. C. Walker and F. Spinale, "The structure and function of the cardiac myocyte: a review of fundamental concepts," *The Journal of Thoracic and Cardiovascular Surgery*, vol. 118, pp. 375–382, 1999.
4. R. F. Schmidt, G. Thews, and F. Lang, *Physiologie des Menschen*. Berlin; Heidelberg; New York: Springer, 2000.
5. "http://chsweb.lr.k12.nj.us."
6. G. Seemann, *Modeling of electrophysiology and tension development in the human heart*. PhD thesis, Karlsruhe Institute of Technology, 2005.
7. D. Goodenough and N. D. Paul, "Beyond the gap: functions of unpaired connexon channels," *Reviews Molecular Cell Biology*, vol. 4, pp. 285–295, 2003.
8. V. Unger, N. Kumar, N. Gilula, and M. Yeager, "Three-dimensional structure of a recombinant gap junction membrane channel," *Science (New York, N.Y.)*, vol. 283, pp. 1176–1180, 1999.
9. R. F. Schmidt, *Physiologie kompakt*. Berlin, Heidelberg, New York: Springer, 1999.
10. "http://www.ceufast.com."
11. A. Kumar, "ECG- simplified," *LifeHugger*, 2010.
12. "http://www.nhlbi.nih.gov/health/health-topics/topics/hhw/."
13. A. R. Houghton, *Making sense of the ECG*. Hodder Education.
14. "http://medical-dictionary.thefreedictionary.com/electrocardiogram."
15. Burton and Cobbe, "Dispersion of ventricular repolarization and refractory period," *Cardiovasc. Res.*, 2001.
16. I. Goldenberg, W. Zareba, and A. Moss, "Long QT Syndrome," *Current Problems in Cardiology*, vol. 33, pp. 629–694, 2008.
17. H. Morita, J. Wu, and D. Zipes, "The QT syndromes: long and short," *Lancet*, vol. 372, pp. 750–763, 2008.
18. M. Walter Allan, *Chapter 12: Long QT Syndrome*.
19. J. Delaney, S. Mittal, and M. Sherrid, "Current perspectives on congenital long QT syndrome," *Anadolu Kardiyoloji Dergisi : AKD = the Anatolian Journal of Cardiology*, vol. 9 Suppl 2, pp. 3–11, 2009.
20. P. Hedley, P. Jorgensen, S. Schlamowitz, R. Wangari, J. Moolman-Smook, P. Brink, J. Kanters, V. Corfield, and M. Christiansen, "The genetic basis of long QT and short QT syndromes: a mutation update," *Human Mutation*, vol. 30, pp. 1486–1511, 2009.
21. L. Crotti, G. Celano, F. Dagradi, and P. Schwartz, "Congenital long QT syndrome," *Orphanet Journal of Rare Diseases*, vol. 3, p. 18, 2008.
22. I. Goldenberg, A. Moss, J. Bradley, S. Polonsky, D. Peterson, S. McNitt, W. Zareba, M. Andrews, J. Robinson, M. Ackerman, J. Benhorin, E. Kaufman, E. Locati, C. Napolitano, S. Priori, M. Qi,

upna Universidad Pública de Navarra Nafarroako Unibertsitate Publikoa
Todos los derechos reservados
Eskubide guztiak erresalbatu dira

P. Schwartz, J. Towbin, G. Vincent, and L. Zhang, "Long-QT syndrome after age 40," *Circulation*, vol. 117, pp. 2192–2201, 2008.

23. O. S. Jespersen T, Grunnet M, "The KCNQ1 potassium channel: from gene to physiological function.," *Physiology (Bethesda)*, 2005.
24. M. Sanguinetti, M. Curran, A. Zou, J. Shen, P. Spector, D. Atkinson, and M. Keating, "Coassembly of K(V)LQT1 and minK (IsK) proteins to form cardiac I(Ks) potassium channel," *Nature*, vol. 384, pp. 80–83, 1996.
25. J. Barhanin, F. Lesage, E. Guillemare, M. Fink, M. Lazdunski, and G. Romey, "K(V)LQT1 and lsK (minK) proteins associate to form the I(Ks) cardiac potassium current," *Nature*, vol. 384, pp. 78–80, 1996.
26. Y. Melman, S. Um, A. Krumerman, A. Kagan, and T. McDonald, "KCNE1 binds to the KCNQ1 pore to regulate potassium channel activity," *Neuron*, vol. 42, pp. 927–937, 2004.
27. The Cardiac Society of Australia and New Zealand, "Guidelines for the diagnosis and management of Familial Long QT Syndrome,"
28. "http://www.nhlbi.nih.gov/health/dci/diseases/qt/qtiagnosis.html."
29. P. J. Schwartz, A. J. Moss, G. M. Vincent, and R. S. Crampton, "Diagnostic criteria for the long QT syndrome. An update," *Circulation*, vol. 88, pp. 782–784, 1993.
30. S. Priori, P. Schwartz, C. Napolitano, R. Bloise, E. Ronchetti, M. Grillo, A. Vicentini, C. Spazzolini, J. Nastoli, G. Bottelli, R. Folli, and D. Cappelletti, "Risk stratification in the long-QT syndrome," *The New England Journal of Medicine*, vol. 348, pp. 1866–1874, 2003.
31. W. Zareba, A. Moss, P. Schwartz, G. Vincent, J. Robinson, S. Priori, J. Benhorin, E. Locati, J. Towbin, M. Keating, M. Lehmann, and W. Hall, "Influence of genotype on the clinical course of the long-QT syndrome. International Long-QT Syndrome Registry Research Group," *The New England Journal of Medicine*, vol. 339, pp. 960–965, 1998.
32. "http://www.daviddarling.info/encyclopedia/l/longtyndrome.html."
33. E. Neher, B. Sakmann, and J. Steinbach, "The extracellular patch clamp: a method for resolving currents through individual open channels in biological membranes," *Pflugers Archiv : European Journal of Physiology*, vol. 375, pp. 219–228, 1978.
34. J. Malmivuo and R. Plonsey, *Bioelectromagnetism. Principles and applications of bioelectric and bio magnetic fields.* New York Oxford: Oxford University Press, 1995.
35. E. P. Scholz, N. Niemer, D. Hassel, E. Zitron, H. F. Burgers, R. Bloehs, C. Seyler, D. Scherer, D. Thomas, S. Kathofer, H. A. Katus, W. A. Rottbauer, and C. A. Karle, "Biophysical properties of zebrafish ether-a-go-go related gene potassium channels," *Biochemical and Biophysical Research Communications*, vol. 381, pp. 159–164, 2009.
36. G. Berecki, J. Zegers, A. Verkerk, Z. Bhuiyan, B. de Jonge, M. Veldkamp, R. Wilders, and A. van Ginneken, "HERG channel (dys)function revealed by dynamic action potential clamp technique," *Biophysical Journal*, vol. 88, pp. 566–578, 2005.
37. K. H. W. J. ten Tusscher, D. Noble, P. J. Noble, and A. V. Panfilov, "A model for human ventricular tissue," *American Journal of Physiology. Heart and Circulatory Physiology*, vol. 286, pp. H1573–89, 2004.
38. K. H. W. J. ten Tusscher and A. V. Panfilov, "Alternans and spiral breakup in a human ventricular tissue model," *American Journal of Physiology. Heart and Circulatory Physiology*, vol. 291, pp. H1088–100, 2006.
39. C. E. Clancy and Y. Rudy, "Na(+) channel mutation that causes both Brugada and long-QT syndrome phenotypes: a simulation study of mechanism," *Circulation*, vol. 105, pp. 1208–1213, 2002.
40. C.Werner, *Simulation der elektrischen Erregungsausbreitung in anatomischen Herzmodellen mit adaptiven zellularen Automaten.* PhD thesis, 2001.
41. A. L. Hodgkin and A. F. Huxley, "A quantitative description of membrane current and its application to conduction and excitation in nerve," *Journal of Physiology*, vol. 117, pp. 500–544, 1952.

upna Universidad Pública de Navarra Nafarroako Unibertsitate Publikoa
Todos los derechos reservados
Eskubide guztiak erresalbatu dira

42. D. U. J. Keller, O. Jarrousse, T. Fritz, S. Ley, O. Dössel, and G. Seemann, "Impact of physiological ventricular deformation on the morphology of the T-wave: a hybrid, static-dynamic approach," *IEEE Trans Biomed Eng.*, vol. 58, pp. 2109–2119, 2011.
43. D. U. J. Keller, F. M. Weber, G. Seemann, and O. Dössel, "Ranking the influence of tissue conductivities on forward-calculated ECGs," *IEEE Transactions on Biomedical Engineering*, vol. 57, pp. 1568–1576, 2010.
44. Y. Pereon, S. Demolombe, I. Baro, E. Drouin, F. Charpentier, and D. Escande, "Differential expression of KvLQT1 isoforms across the human ventricular wall," *Am J Physiol Heart Circ Physiol*, vol. 278, p. 1908, 2000.
45. D. U. J. Keller, D. L. Weiss, O. Dössel, and G. Seemann, "Influence of IKs Heterogeneities on the Genesis of the T-Wave: A Computational Evaluation," *IEEE Trans Biomed Eng.*, p. in print, 2011.
46. G. Seemann, F. B. Sachse, M. Karl, D. L. Weiss, V. Heuveline, and O. Dössel, "Framework for modular, flexible and efficient solving the cardiac bidomain equation using PETSc," *Mathematics in Industry*, vol. 15, pp. 363–369, 2010.
47. D.-W. Liu and C. Antzelevitch, "Characteristics of the delayed rectifier current (IKr and IKs) in canine ventricular epicardial, midmyocardial, and endocardial myocytes," *Circulation Research*, vol. 76, pp. 351–365, 1995.
48. N. Szentadrassy, T. Banyasz, T. Biro, G. Szabo, B. I. Toth, J. Magyar, J. Lazar, A. Varro, L. Kovacs, and P. P. Nanasi, "Apico-basal inhomogeneity in distribution of ion channels in canine and human ventricular myocardium," *Cardiovasc Res*, vol. 65, pp. 851–860, 2005.
49. C. G. K. L. E. Drouin, F. Charpentier and H. L. Marec, "Electrophysiological characteristics of cells spanning the left ventricular wall of human heart: Evidence for the presence of M Cells," *J. Am. Coll. Cardiol.*, 1995.
50. A. Khawaja, S. Sanyal, and O. Dössel, "A wavelet-based technique for baseline wander correction in ECG and multi-channel ECG," *IFMBE Proc*, 2005.
51. "http://www.medscape.com."
52. D. U. J. Keller, G. Seemann, D. L. Weiss, D. Farina, J. Zehelein, and O. Dössel, "Computer based modeling of the congenital long-QT syndrome in the Visible Man torso: From genes to ECG," pp. 1410–1413, 2007.
53. F. G. Yanowitz, "Lesson III. Characteristics of the Normal ECG," *University of Utah School of Medicine*, 2010.
54. M. Fitz, "Loyola university chicago stritch school of medicine > medicine i." 2010.
55. "http://www.ecglibrary.com."
56. R. E. Klabunde, "Image for cardiovascular physiology concepts > electrocardiogram (ekg, ecg).".

upna Universidad Pública de Navarra Nafarroako Unibertsitate Publikoa
Todos los derechos reservados
Eskubide guztiak erresalbatu dira

upna Universidad Pública de Navarra Nafarroako Unibertsitate Publikoa
Todos los derechos reservados
Eskubide guztiak erresalbatu dira